



Cite this: RSC Adv., 2015, 5, 76229

Noble metal@metal oxide semiconductor core@shell nano-architectures as a new platform for gas sensor applications

Prabhakar Rai,^{*a} Sanjit Manohar Majhi,^b Yeon-Tae Yu^b and Jong-Heun Lee^{*cd}

Among the complex nanostructures, core@shell nanomaterials are gaining much attention, as the physical properties of the core and shell can be easily and separately tuned. Two materials in the form of core@shell nanostructures combine their individual properties and also bring unique properties in comparison with single-component materials. Recently, the formation of core@shell nanoparticles (NPs) having noble metals (Au, Ag, Pt and Pd) as a core and metal oxides semiconductors (TiO_2 , SnO_2 , and Cu_2O) as a shell has attracted immense research interest in sensing, photo-catalysis, dye-sensitized solar cells and so on due to tailorability and functionality in the core and shell. Therefore, an overview of the advances in this exciting field of noble metals@metal oxides core@shell NPs has been presented in this feature article. It includes systematic synthesis approaches of noble metal@metal oxide core@shell NPs and their applications in the field of gas sensors, which is based on the literature and our own recent work. The synthesis of core@shell NPs with controllable sizes, compositions, morphologies, structures and functionalities has been presented considering the advantages and the demerits of the process. Applications of these core@shell NPs in the areas of gas sensing and their sensing mechanisms are discussed. The future prospects of such core@shell nanostructures for gas sensing applications are also highlighted.

Received 20th July 2015
 Accepted 28th August 2015

DOI: 10.1039/c5ra14322e
www.rsc.org/advances

^aDepartment of Chemical Engineering, Indian Institute of Technology Kanpur, Kanpur 208016, India. E-mail: prkrai@iitk.ac.in

^bDivision of Advanced Materials Engineering and Research Centre for Advanced Materials Development, College of Engineering, Chonbuk National University, Jeonju 561-756, Republic of Korea

^cDepartment of Materials Science and Engineering, Korea University, Anam-Dong 5-1, Seoul 136-713, South Korea. E-mail: jongheun@korea.ac.kr

^dDepartment of Chemical and Materials Engineering, King Abdulaziz University, Jeddah 21589, Saudi Arabia



Prabhakar Rai is INSPIRE Faculty in the Department of Chemical Engineering at the Indian Institute of Technology Kanpur, India. Previously, he was Research Professor in the Department of Materials Science and Engineering at Korea University and Assistant Research Professor in the Department of Informatic Electronic Materials Engineering at Chonbuk National University,

South Korea. He received his Doctoral degree in Informatic Electronic Materials Engineering, in 2012, at Chonbuk National University, South Korea and M.Sc. degree in Inorganic Chemistry at the University of Allahabad, India. His research is mainly focused on synthesis of nanoscale noble metals@metal oxides core@shell nanostructures for the gas sensor applications.



Sanjit Manohar Majhi is currently pursuing his doctoral course in the Department of Informatic Electronic Materials Engineering at Chonbuk National University, South Korea. He received his M.Sc. degree in Chemistry, in 2008, at Utkal University, India. He has worked as a researcher from 2009–2012, at the Institute of Minerals and Materials Technology (IMMT), CSIR, Bhubaneswar, India. His research interests include the synthesis of noble metal nanoparticles and metal oxide semiconductors to design core@shell nanostructures for the gas sensor applications.

1. Introduction

Atmospheric pollution resulting from gaseous pollutants has caused major concerns such as human health issues, acid rain, ozone depletion and the greenhouse effect.¹ Thus, gas sensors have become a crucial part of modern life with applications in environmental monitoring and personal safety, which are increasingly being integrated into mass-market applications, for instance in air quality control in buildings and motor vehicles, as well as the more traditional areas of toxic and explosive gas detection. There are various types of detectors available in the market having the same function *i.e.* to monitor and warn of a dangerous gas level. Among them, chemiresistive metal oxide semiconductor (MOS) sensors are most investigated because of their high sensitivity, small size, low cost and easy maintenance.² In 1962 Seiyama *et al.*³ proposed the idea of gas sensing, where adsorption and desorption of gases cause electrical changes, using ZnO thin films. The other commonly used sensor material, SnO₂, was proposed as a gas sensor in the same year by Taguchi,⁴ and since 1968 these sensors have been commercially available through Figaro Engineering.⁵ Other metal oxides such as n-type (Fe₂O₃, In₂O₃, TiO₂, and WO₃) and p-type (CuO, NiO, Co₃O₄, and Cr₂O₃) metal oxides have also been explored as gas sensors.⁶

The receptor and transducer functions are two major key functions involved in gas sensing by chemiresistive MOS devices (Fig. 1).⁷ The receptor function induces an electronic change on the oxide surface through a gas–solid interface, which results in the recognition of a target gas. The transducer function involves the transduction of the surface phenomenon into an electrical resistance change of the sensor. Thus, the gas sensing mechanism of metal oxides involves change in resistance of the sensor, caused by the chemical adsorption and/or the reaction of test gas molecules on the surface of the sensing materials (Fig. 2). In n-type MOS, oxygen molecules adsorb on the surface and then form the charged chemisorbed

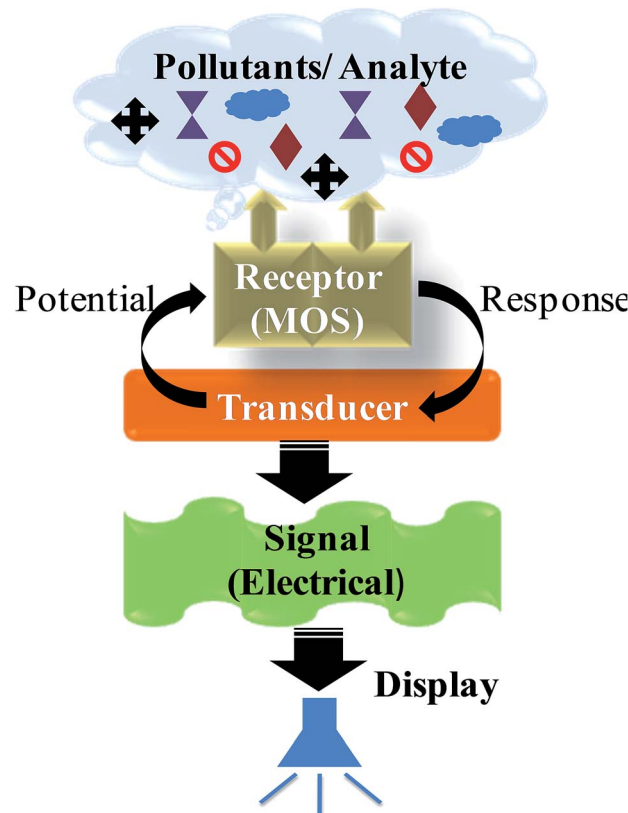


Fig. 1 Schematic showing the working principles of gas sensors.

oxygen species (O_2^- , O^- or O^{2-}) by capturing free electrons from the conduction band of MOS. It results in decrease in electron density of sensing materials, and therefore electron depletion layers is formed on the surface of sensing materials as shown schematically in Fig. 2a. When the sensors were exposed gaseous atmosphere, such as CO, the gas molecules would react with adsorbed oxygen species on the surface of MOS ($2CO_{(g)} +$



Yeon-Tae Yu is a Professor in the Division of Advanced Materials Engineering at Chonbuk National University. He received his engineering diploma in Department of Metallurgy Engineering in 1988 from Chonbuk National University, South Korea and a Doctoral degree (1993) from Tohoku University, Japan. From 1993 to 2003, he was a Senior Researcher at the Korea Institute of Geoscience and Mineral Resources. In 2004, he moved to the Division of Advanced Materials Engineering of Chonbuk National University as an Assistant Professor. His main research interests are the synthesis of core–shell structure composite nanoparticles and their application for gas sensors.



Jong-Heun Lee has been a Professor in the Department of Materials Science and Engineering at Korea University since 2003. He received his B.S., M.S. and Ph.D. degrees from Seoul National University in 1987, 1989 and 1993, respectively. Between 1993 and 1999, he developed automotive air-fuel ratio sensors at the Samsung Advanced Institute of Technology. He was a STA fellow at the National Institute for Research in Inorganic Materials (currently NIMS, Japan) from 1999 to 2000 and a Research Professor at Seoul National University from 2000 to 2003. His current research interests include chemical sensors and functional nanostructures.

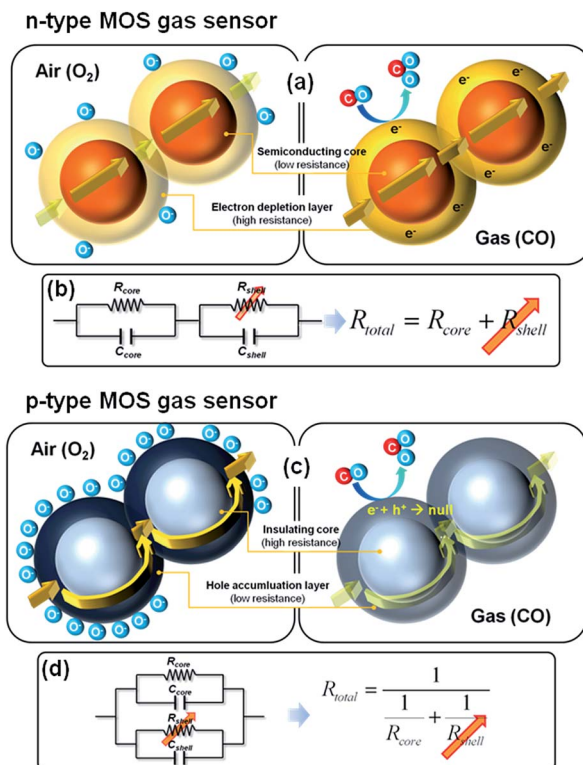


Fig. 2 Schematic showing gas sensing mechanisms of (a and b) n-type MOS and (c and d) p-type MOS. Reprinted with permission from ref. 6. Copyright 2014 Elsevier.

$2O_{(ads)}^- \leftrightarrow 2CO_{(g)} + 2e^-$). As a result, the trapped electrons were released back to the conduction band of MOS, which eventually led to a remarkable decrease of resistance. The serial connection between semiconducting core and resistive shell can be given as an equivalent circuit (Fig. 2b). In p-type MOS, the oxygen adsorption with negative charge electrostatically attracts the holes, which forms hole accumulation layer near the surface (Fig. 2c). The conduction can be explained by the parallel competition between those along semiconducting thin shells and through resistive cores (Fig. 2d). When the sensors were exposed to CO, the electron generated by the reaction between CO and $O_{(ads)}^-$ decrease the near-surface hole concentration by electron hole combination reaction, which increase the sensor resistance. These change of resistance in n-type and p-type MOS can be used for the signal of presence of gas through alarm.

Bare metal oxides are itself active for this function, however this function can be boost to induce a large change in sensitivity by adding additive (noble metals, acidic or basic oxides) to the metal oxide surface.⁸ Thus, the deposition of a catalyst on metal oxide accelerates the reaction and to increase the sensitivity of MOS gas sensors. The catalyst also influences the selectivity of sensor.⁹ Therefore, noble metal additives are commonly used as activators or sensitizers to improve/tune the gas selectivity, sensitivity and to lower the operating temperature.^{10,11} There are two ways in which the catalysts can affect the inter-granular contact region and hence affect the film resistance (Fig. 3).

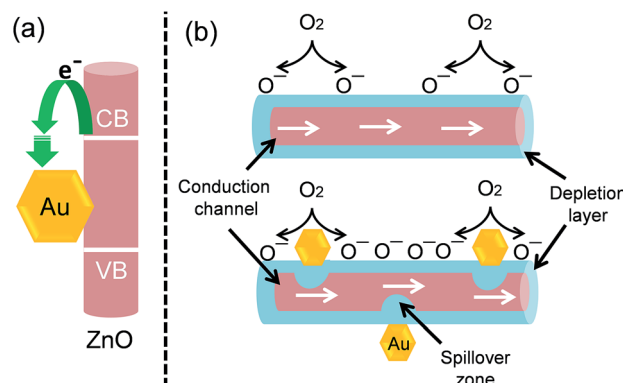


Fig. 3 Schematic showing (a) electronic and (b) chemical sensitization of noble metals.

One is the spillover mechanism or chemical sensitization and other is Fermi energy control or electronic sensitization.¹² In chemical sensitization, noble metals catalytically activate the dissociation of molecular oxygen, which then adsorb on the metal oxide surface by capturing conductance band electrons. It results in a greater degree of electron withdrawal from the metal oxide than for the bare metal oxide. In electronic sensitization, noble metal acts as an electron acceptor on semiconductor oxide surfaces, which results in increase of the depletion layer.¹³ Therefore, the change in resistance in noble metals loaded metal oxide is larger as compared with the bare metal oxides, which results in increase in gas response. Thus, noble metal helps in the improvement of sensing performance.

Traditionally, surface modification of metal oxides involves the deposition of noble metals on metal oxide surface. However, this exercise passivates the effective surface area of metal oxides involved in gas sensing. Also, noble metal NPs are unstable against heating, which results in a loss of catalytic activity mainly because of the increased mobility of the metal NPs on the support at higher temperatures.¹⁴ The mobility of metal NPs on oxide support results in the formation of either a shunting layer or an active membrane filter, which effectively obstruct the penetration of the targeting gas into the surface of the gas sensing matrix. The poisoning of noble metal NPs many by many chemicals that contain sulfur (H_2S , SO_2 , and thiols) or phosphorus is another problem of their application.¹⁵ Therefore, it was challenging, until the emergence of core@shell structure, to overcome above disadvantages along with improvement in performance and stability of sensor. Recent studies have shown that core@shell structured materials with tailored physical and chemical properties, in both the cores and shells, provide powerful platforms for nanoreactors, drug/gene delivery, lithium-ion batteries, biosensors, photocatalysis, surface-enhanced Raman scattering etc.¹⁶⁻²⁰ The coating is mainly used to modify its optical properties²¹ as well as passivate the core chemically,²² or as a size selective membrane for catalytic processes at the core surface.²³ In case of noble metal@metal oxide core@shell, the formation of Schottky barrier due to large difference between the intrinsic Fermi level of the core and the conduction band energy of the

semiconductor shell results in the trapping of mobile electrons in core that diffuse within the shell. Transfer of stored charge to solution phase acceptors will be retarded if the trapping energy $E_{tr} = E_f(\text{core}) - E_{cb}(\text{shell}) \gg kT$. Therefore, the properties can be modified by changing core or shell materials or the core to shell ratio.²⁴ The coating of shell material increases the overall particle stability and dispersibility of the core particle due to decrease in reactivity and increase in thermal stability. Such a metal@semiconductor particle has shown potential applications in gas sensor as reported by our research group.²⁵ Since then, plenty of research papers have been published by many researchers including us on application of core@shell NPs for gas sensor applications, indicating that the core@shell structured materials are already receiving increasing commercial attention. A large number of synthesis approaches are also available in literature for the preparation of noble metal@metal oxide core@shell structures. A review article on the synthesis and applications of different core@shell NPs are published by Chaudhuri *et al.*¹⁶ Many researchers have also demonstrated the fact that core@shell NPs are widely used in different applications.^{26–29} However, reviews outlining the utilization of noble metal@metal oxide core@shell NPs in gas sensing have not been available. Therefore, in this feature article we have focused on recent research progress in metal@metal oxides core@shell NPs for gas sensor applications. Based on published works in the literature and some of our own recent works on noble metal@metal oxide core@shell NPs, we have presented a systematic synthesis approaches for the preparation of core@shell NPs and their gas sensing applications in this review. This overview is mainly organized in two sections. In the first section, we present the key synthetic strategies for controlling the size, composition, geometry, structure and functionalization of core@shell NPs by discussing some representative core@shell NPs as examples. In the second section, the applications of core@shell NPs in gas sensing fields are reviewed. Finally, we provide some perspectives on the future developments and directions of the synthesis, characterization and application of core@shell NPs.

2. Synthesis approaches

The formation of noble metal@metal oxides core@shell NPs requires the control of several processes, such as nucleation and growth of the shell material on noble metal seeds. These processes are influenced by a number of factors, such as time, temperature, concentration, synthesis methods, lattice mismatch, interfacial energy, surfactant *etc.* Typically, the lattice mismatch and lack of chemical interaction between noble metals and metal oxides often results in large interfacial energy between an oxide and a metal. If there is lattice mismatch between two materials then it is hard to synthesize their core@shell configuration. However, ligand/surfactant can be used to tune the interface between two materials. Noble metal@silica core@shell NPs is relatively well-known, however this method has not been extensively applied to other oxide coatings, mainly because of aggregation problems.³⁰ Syntheses of many metal oxides, except for silica, require the use of metal

salts as precursors, which could cause aggregation of the seed NPs. However, if the use of metal salts is unavoidable, the use of suitable ligand or surfactant can be the best strategy to form core@shell NPs. The selection of a compatible ligand/surfactant is challenging, and therefore there are only few reports about the synthesis of core@shell NPs metal oxides, although their corresponding pure oxides NPs are common. This is possibly the reason why the core@shell NPs of noble metals with metal oxides is case specific. Therefore, we are going to discuss the synthesis of specific metal@metal oxide core@shell NPs, especially those materials used for gas sensing.

2.1 Core@shell NPs

2.1.1 Metal@TiO₂ core@shell NPs. The first attempt of formation of metal@TiO₂ core@shell NPs was carried out on Au NPs by sol-gel method, where Au NPs were synthesized first followed by the deposition of TiO₂ shell on Au NPs.^{31,32} However, in these methods well defined core@shell NPs were not formed. The formation of well-defined TiO₂ shell on noble metal core was first reported by Li *et al.* as shown in Fig. 4.³³

The Au@TiO₂ core@shell NPs (500–800 nm) were synthesized in two steps, which involved the deposition of TiO₂ shell (200–500 nm) on initially formed Au NPs core (50–150 nm) by hydrothermal method. The ascorbic acid facilitated the formation of well-faceted and large anatase TiO₂ crystallites, whereas CTAB developed well-faceted Au cores. Hollow Au@TiO₂ core@shell NPs were also formed through Ostwald ripening which involved solid evacuation of central TiO₂ crystallites as shown in Fig. 4b. In addition, the size of the Au core (150–250 nm) within the nanoreactor was further tuned through the reduction of gold nutrients in HAuCl₄-soaked Au@TiO₂ nanoreactors (Fig. 4c), which involved slow inter diffusion between the HAuCl₄ inside the nanoreactor and the CTAB/ascorbic acid

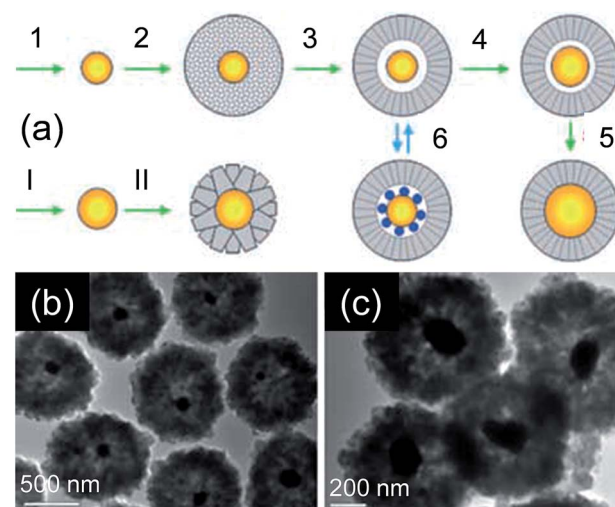


Fig. 4 (a) Schematic illustration of Au@TiO₂ nanoreactor formation and size tuning of core catalyst, (b) TEM images of Au@TiO₂ core@shell nanoreactors with a central vacant space (prepared in step 3 of (a), and (c)) after enlargement of Au cores (prepared in step 4 of (a)), reprinted with permission from ref. 33 Copyright 2005 Wiley-VCH.

solution outside the nanoreactor. Our research group has extended this method for the synthesis of M(Au, Ag, Pt)@TiO₂ core shell NPs and size and shape of core and shell materials was tuned by controlling the concentration of precursors (Fig. 5a–d).³⁴

In our study, M@TiO₂ core@shell NPs with truncated wedge-shaped TiO₂ morphology have been formed due to the epitaxially segmented orientation growth of individual TiO₂ antenna for single Au@TiO₂ core@shell NPs (Fig. 5e). It revealed the epitaxial formation of (101) crystal planes of TiO₂ near the Au-TiO₂ interface due to matching with exposed Au (111) planes which kept interfacial energy low. It was found that there was a change in growth direction from core to rim region and external region of TiO₂ antenna preferentially grew along the [001] direction. The formation of well-defined wedge-like TiO₂ shells with externally exposed truncated crystal {004} facets was dependent on the F⁻ ions concentration (produced from hydrolyzed TiF₄ precursors). It has been found that the use of microwave resulted in rapid synthesis of Au@TiO₂ core@shell NPs at low temperature (at 100 °C for 1 h).^{35,36} This is because microwave dielectric heating is rapid and it is possible to heat the whole reaction mixture without any temperature gradient. No phase transition in either TiO₂ or Au was found and their shape and size was also maintained even after sintering at 900 °C. It is unusual that anatase phase of TiO₂ was maintained at 900 °C, because most study shows that anatase phase change

to rutile when calcined at >500 °C.³⁷ We have suggested that the inhibition of the transition was related to the stabilization of the anatase phase by the surrounding Au NPs through the formation of Ti–O–Au bonds at the interface.^{38,39} Interestingly, Au@TiO₂ core@shell hollow submicrospheres have been formed when water was replaced by ethanol under hydrothermal condition because ethanol can accelerate both the formation process of amorphous Au@TiO₂ solid microspheres and the subsequent Ostwald ripening process.⁴⁰ As compared to centric core@shell NPs, Seh *et al.*⁴¹ reported the synthesis of eccentric Au@TiO₂ core@shell nanostructures *via* sol-gel method as shown in Fig. 6.

The formation of eccentric core@shell structures involved plane-selective condensation of TiO₂ onto citrate-capped Au cores. It has been found that citrate ions bind more strongly to the (111) planes as compared to the (110) or (200) planes of noble metals. Therefore, hydrolyzed titanium alkoxide precursor has easily displaced weakly-bound citrate ions on the (110) and (200) planes as compared to strongly-bound citrate ions on the (111) planes, leading to the eccentric core@shell structure (Fig. 6d). Liu *et al.*⁴² reported the synthesis of Au@TiO₂ core@shell NPs with controlled shell thickness on having various shape and size of Au NPs core and applied for DSSC. Recently, Goebl *et al.*⁴³ has reported sol-gel process to coat gold NPs with TiO₂ to produce Au@TiO₂ core@shell catalyst particles, which can be rendered crystalline *via* calcinations at high temperatures. Several researchers^{44–50} tried to synthesize other M@TiO₂ core@shell NPs other than Au@TiO₂ core@shell NPs. In most cases TiO₂ shell layer was porous, and therefore these materials would be very useful platforms for sensing and catalytic applications.^{34–36,41}

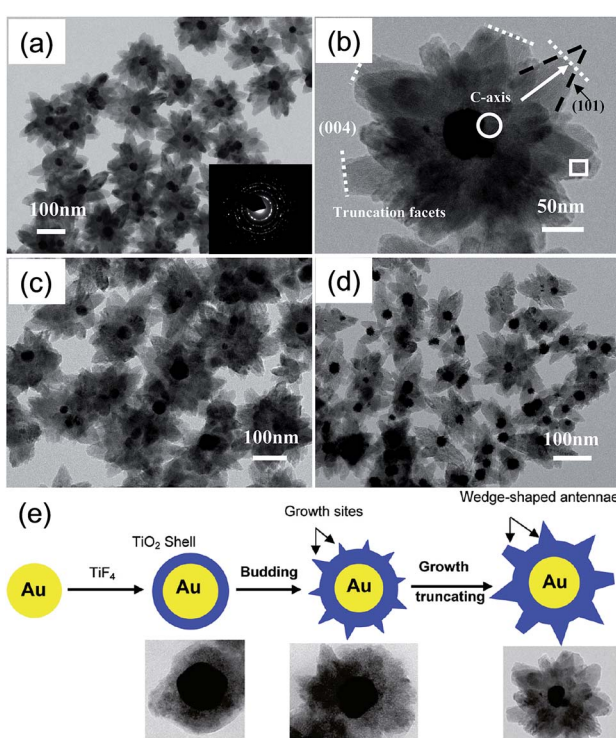


Fig. 5 TEM images of the as-prepared core–shell Au@TiO₂ core@shell NPs (a) and individual particle image (b), Ag@TiO₂ NPs (c), Pt@TiO₂ NPs (d), and schematic diagram of the proposed formation process of core-shell Au@TiO₂ core@shell NPs with truncated wedge-shaped morphology (e), reprinted with permission from ref. 34. Copyright 2009 American Chemical Society.

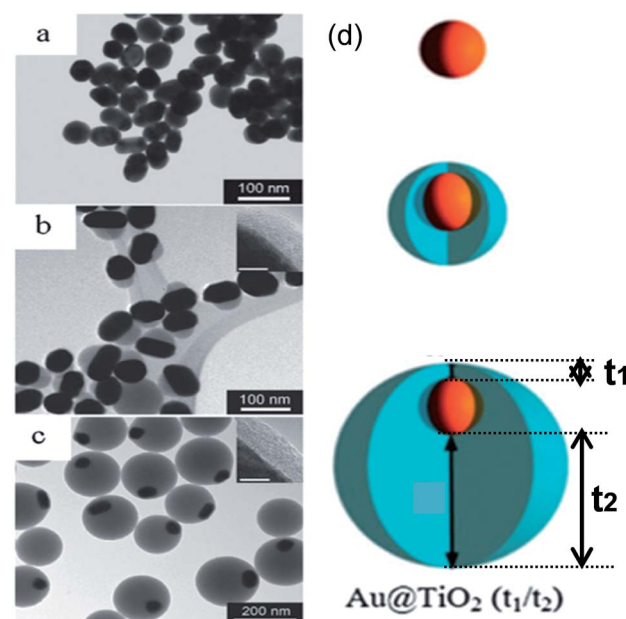


Fig. 6 (a–c) TEM images of (a) 50 nm Au cores, (b) Au@TiO₂ (5/25) and (c) Au@TiO₂ (5/125) nanostructures. The thinner sides of the TiO₂ shells are shown (insets) for (b) and (c). Scale bars of inset = 5 nm. (d) Schematic of shell formation, reprinted with permission from ref. 41. Copyright 2011 Royal Society of Chemistry.

2.1.2 Metal@SnO₂ core@shell NPs. The synthesis of metal@SnO₂ core@shell NPs was first reported by Mulvaney and co-workers⁵¹ where aqueous chemical techniques were employed to synthesize citrate-stabilized Au colloids homogeneously coated with SnO₂ NPs. Our research group^{52,53} has also synthesized Au@SnO₂ core@shell NPs using microwave-assisted hydrothermal method and its physical properties were compared with Au@SnO₂ synthesized by aqueous chemical techniques. The shape and size of Au@SnO₂ core@shell NPs synthesized by both methods were similar except the deposition time of the SnO₂ shell on the surface of the Au NPs was faster in microwave heating than that with the aqueous chemical techniques. Microstructures achieved by two-dimensional TEM characterization showed that both samples maintained the similar core@shell structures with their sizes ranging between 30–50 nm (Fig. 7).

However, it was difficult to control the shell thickness in these methods and free SnO₂ NPs were formed with increasing stannate concentration. The thickness and density of the oxide shell Au@SnO₂ core@shell NPs was controlled by Tripathy *et al.*⁵⁴ using sonochemical method by adjusting sodium stannate concentration. Several other researchers have also attempted to synthesize Au@SnO₂ core@shell NPs *via* different techniques. Yu *et al.*⁵⁵ synthesized Au@SnO₂ by intermetallics-based dry oxidation method, where SnO₂ shell was grown directly from one component of the intermetallics (AuS) by selective oxidation. Au NPs with a mean size of *ca.* 15 nm were uniformly encapsulated by the SnO₂ shell. The thickness of the shell was 6–7 nm, and the final size of the Au@SnO₂ NPs was in accordance with the AuSn NPs. Colloidal technique has been reported by Patra and co-workers⁵⁶ to synthesize Au@SnO₂ core@shell NPs. Meanwhile, core@shell NPs of SnO₂ with other noble metals except gold have not achieved similar success and in most cases well defined core@shell NPs were not formed.^{57–60}

2.1.3 Metal@ZnO core@shell NPs. The formation of core@shell NPs of SnO₂ and TiO₂ was relatively more

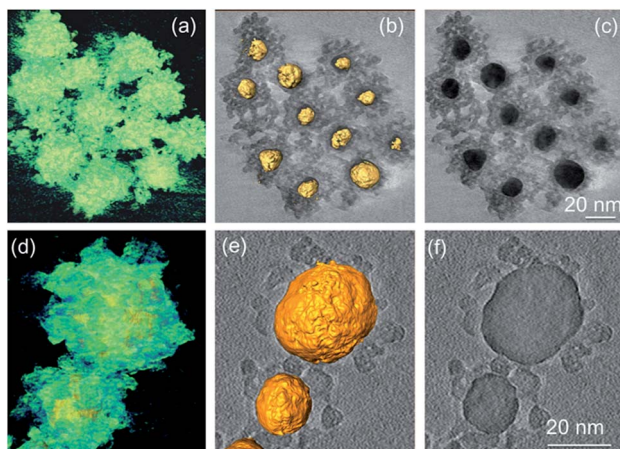


Fig. 7 3D reconstructed volumes and sliced images of Au@SnO₂ core@shell NPs prepared by (a)–(c) precipitation method and (d)–(e) microwave-assisted hydrothermal method. Reprinted with permission from ref. 53. Copyright 2012 Elsevier.

convenient as both of them cubic structure similar to noble metals, and therefore, there has been good lattice match for core@shell formation. However, ZnO is hexagonal structure and preferentially grows along c-axis, therefore difficult to deposit on noble metals to form core@shell structure. Thus, the formation of metal@ZnO core@shell NPs was challenging due to lattice mismatch between noble metals and ZnO and neither a ligand nor a surfactant alone can solve the encapsulation problem.⁶¹ Therefore, the synthesis of such core@shell nanostructures has not been reported, although eccentric or Janus (two-faced) Au-ZnO NPs were known.^{62–64} Fan *et al.*⁶³ demonstrated a seed mediated method that spontaneously achieves facet-selective growth of ZnO nanorods on {111} rather than {100} facets of Ag nanocrystals (Fig. 8). This is because {111} facet of Ag has hexagonal symmetry, which is similar to the basal {0001} facet of hexagonal ZnO with a mismatch of only 2.68% as compared to 23.9% mismatch with {100} facet having square close-packed arrangement. Therefore, the {111} facet with a better structure match was more favorable for the nucleation and growth of ZnO.

Several researchers^{65–67} have also attempted to prepare well defined core–shell Ag@ZnO NPs. However, these were preliminary studies without in-detailed information on the formation mechanism of core@shell NPs. More recently, Sun *et al.*⁶⁸ successfully synthesized metal@ZnO core@shell NPs with well-defined morphology and presented a detailed growth mechanism (Fig. 9).

It has been found that the polyvinylpyrrolidone (PVP) and 4-mercaptopbenzoic acid used in the synthesis of Au@ZnO played

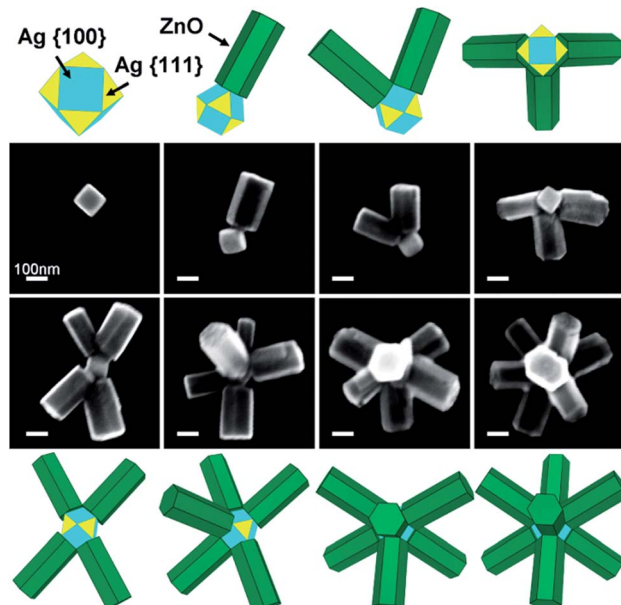


Fig. 8 SEM images showing the selective growth of different numbers of ZnO nanorods on the {111} facets of Ag truncated nanocubes. The corresponding geometrical models of the heterogeneous nanostructures are presented. The yellow and cyan color in schematic of Ag crystal represent the {111} and {100} facets of Ag, respectively. The green color represent the facets of the ZnO nanorods. Reprinted with permission from ref. 63. Copyright 2009 American Chemical Society.

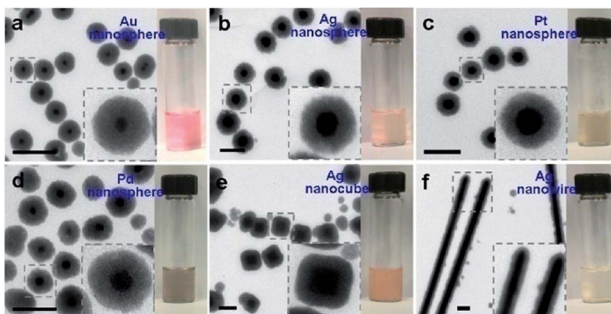


Fig. 9 TEM images and photographs of metal@ZnO NPs that were synthesized from different noble metal cores: citrate-stabilized NPs, including (a) Au nanospheres ($d_{\text{Au}} = 15 \text{ nm}$); (b) Ag nanospheres ($d_{\text{Ag}} = 60 \text{ nm}$); and (c) Pt nanospheres ($d_{\text{Pt}} = 40 \text{ nm}$); and PVP-stabilized NPs, including (d) Pd nanospheres ($d_{\text{Pd}} = 20 \text{ nm}$); (e) Ag nanocubes ($d_{\text{Ag}} = 150 \text{ nm}$); and (f) AgNWs ($d_{\text{AgNW}} = 120 \text{ nm}$, $l_{\text{AgNW}} = 3\text{--}5 \mu\text{m}$). Insets show magnified views of typical NPs. Scale bar: 200 nm. Reprinted with permission from ref. 68. Copyright 2013 American Chemical Society.

an important role. They found that 4-mercaptopbenzoic acid can reduce the Au-ZnO interfacial energy.⁶⁹ However, in the absence of PVP, ZnO did not interact well with the hydrophobic ligands on the Au surface indicating that the amphiphilicity of PVP was essential in the ZnO encapsulation when hydrophobic ligands were used. This method was further extended to include Fe_3O_4 , MnO , Co_2O_3 , TiO_2 , Eu_2O_3 , Tb_2O_3 , Gd_2O_3 , $\beta\text{-Ni(OH)}_2$, ZnS , and CdS as the shell materials, demonstrating the versatile nature of coating (Fig. 10).

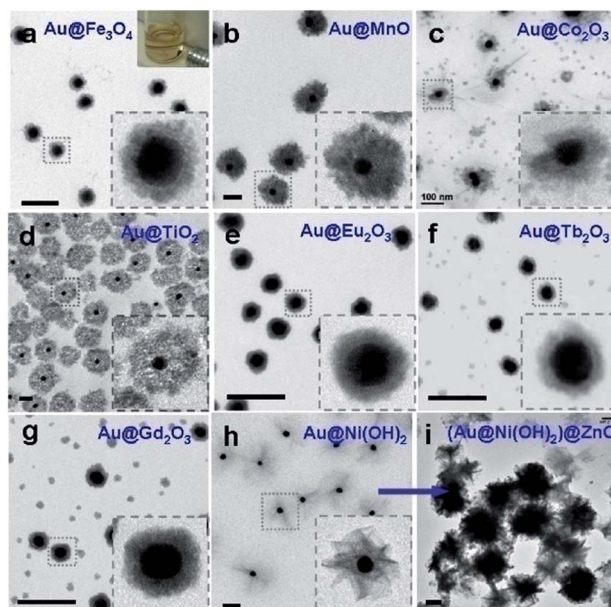


Fig. 10 TEM images of the Au@oxide NPs ($d_{\text{Au}} = 40 \text{ nm}$) with different kinds of oxide shells: (a) $\text{Au@Fe}_3\text{O}_4$, (b) Au@MnO , (c) $\text{Au@Co}_2\text{O}_3$, (d) Au@TiO_2 , (e) $\text{Au@Eu}_2\text{O}_3$, (f) $\text{Au@Tb}_2\text{O}_3$, (g) $\text{Au@Gd}_2\text{O}_3$, (h) Au@Ni(OH)_2 , and (i) $(\text{Au@Ni(OH)}_2)@\text{ZnO}$. Insets show magnified views of typical NPs. Scale bar: 200 nm. Reprinted with permission from ref. 68. Copyright 2013 American Chemical Society.

Similar strategy was applied by Yang *et al.*⁷⁰ to synthesize metal@ZnO core@shell NPs using ascorbic acid to induce deposition of ZnO on various shaped and structured cationic-surfactant-capped NP surfaces, where metal was Au, Ag, Pt, Pd and their bimetallics, such as Au@Ag , Pd@Au , Pd@Pt , Au@Pt etc. This strategy can be directly used to coat CTAB or CTAC metal NPs prepared in water phase (Fig. 11a–x). Oil-soluble NPs prepared in organic solvent can also serve as effective seeds for preparing M@ZnO NPs after they are transferred to water with

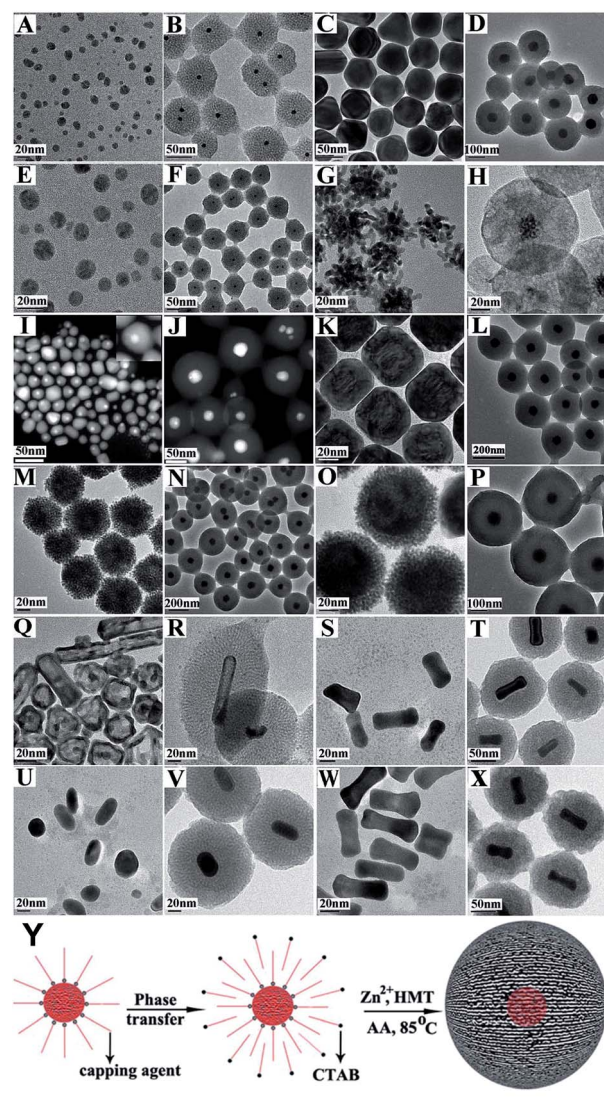


Fig. 11 The typical TEM and HAADF images of seeds and corresponding M@ZnO NPs: (A and B) 15 nm Ag NPs and Ag@ZnO; (C and D) 50 nm Au NPs and Au@ZnO; (E and F) Pd NPs and Pd@ZnO; (G and H) Pt nanodendrites and Pt@ZnO; (I and J) Au@Ag NPs and Au@Ag@ZnO; (K and L) Pd@Au NPs and Pd@Au@ZnO; (M and N) Pd@Pt NPs and Pd@Pt@ZnO; (O and P) Au@Pt NPs and Au@Pt@ZnO; (Q and R) hollow Au/Ag nanostructures and Au/Ag@ZnO; (S and T) Au@Ag nanorods and Au@Ag@ZnO; (U and V) short Au nanorods and Au@ZnO; (W and X) dogbone-like Au nanorods and Au@ZnO; (Y) the coating of hydrophobic NPs with ZnO. Reprinted with permission from ref. 70. Copyright 2013 Royal Society of Chemistry.

CTAB as shown in Fig. 11z. It has been reported that ascorbic acid and CTAB act as templates, which block the continuous growth of ZnO, and therefore large sized single crystalline products cannot form. Three dimensional Au@ZnO core@shell NPs were also synthesized having ZnO nanorods grown radially on Au NPs cores.^{71,72} Many more reports on the synthesis of Au@ZnO core@shell NPs has been published in recent times.^{73,74}

2.1.4 Metal@Fe₃O₄/Fe₂O₃ core@shell NPs. Core@shell NPs having combined functions of magnetic and optical properties from the two components are getting great attention due to exciting opportunities for integrated imaging, diagnosis, targeted drug delivery, and therapeutics. A few reports about Au@Fe₃O₄,^{75,76} Ag@Fe₃O₄ (ref. 77) or Au@MnO⁷⁸ NPs demonstrate this possibility. Jiang *et al.*⁷⁹ reported the synthesis of superparamagnetic Ag@Fe₃O₄ core@shell nanospheres by a facile one-pot hydrothermal method as shown in Fig. 12a–d.

The Ag cores (50 nm) were irregular in shape and were well wrapped by the Fe₃O₄ shell (70 nm). It was demonstrated that the Ag core was produced at the beginning of the reaction followed by the deposition of Fe₃O₄ shell (Fig. 12e). During the ripening, the amorphous Fe₃O₄ transformed to polyhedron-like nanocrystals and thus the mesopores were produced due to the loose packing of the Fe₃O₄ nanocrystals. Similarly, Zhang *et al.*⁸⁰

demonstrated a convenient one-step solvothermal strategy of Ag@Fe₃O₄ core@shell nanostructures. It has been demonstrated that Ag NPs were formed first, which have served as the *in situ* seeds for the successive catalytic reduction, leading to the growth of outer Fe₃O₄ shells. Since the standard potential of Ag⁺/Ag⁰ is higher than that of Fe³⁺/Fe²⁺, the reduction rate of Ag⁺ to Ag⁰ was faster than that of Fe³⁺ to Fe²⁺ and Ag cores are initially formed. Furthermore, this method was also employed to prepare Au@Fe₃O₄ core@shell nanostructures simply by replacing AgNO₃ with HAuCl₄. Recently, Knobel and his co-workers⁸¹ reported the synthesis of brick-like Ag@Fe₃O₄ core@shell NPs using single-step thermal decomposition of iron, with the presence of silver seeds formed in the same reaction mixture (Fig. 13). The role of the temperature pause was essentially to divide the Ag and the iron oxide production inside a single reaction, avoiding the necessity of manipulation and the time consuming gap between steps (Fig. 13a). However, thermal stability of these core@shell NPs in air has not been examined in these literatures. It is well known that heating of Fe₃O₄ in air results in α-Fe₂O₃, therefore, it is possible to convert these M@Fe₃O₄ core@shell NPs into their corresponding Fe₂O₃ core@shell NPs.⁸² Synthesis of core@shell metal@Fe₂O₃ NPs was also reported by many researchers, however they are not of our interest, as they are specific case and their formation mechanism has not been discussed in detail.^{83–88}

Yolk@shell metal@iron oxide has also been reported by several researchers. For example, gold (core)/iron oxide (hollow shell) NPs were prepared by Shevchenko *et al.*⁸⁹ The addition of oleic acid to the reaction mixture changes the morphology of the gold@iron oxide core@hollow-shell NPs, leading to more uniform shells formed around the gold cores. Wei *et al.*⁹⁰ synthesized a uniform multifunctional nanostructure,

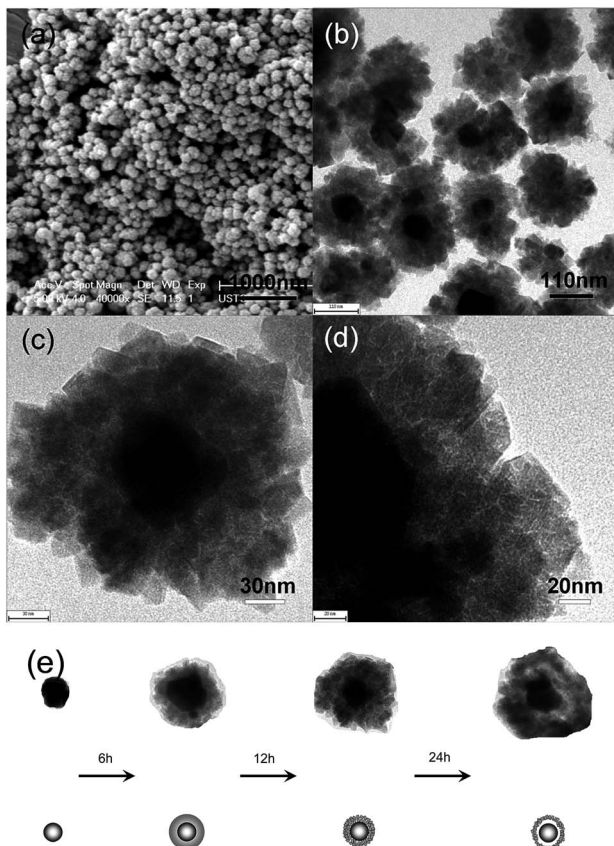


Fig. 12 (a) SEM image, (b, c and d) TEM images and (e) a schematic illustration of the formation of the Ag@Fe₃O₄ core@shell nanospheres. Reprinted with permission from ref. 79. Copyright 2012 Royal Society of Chemistry.

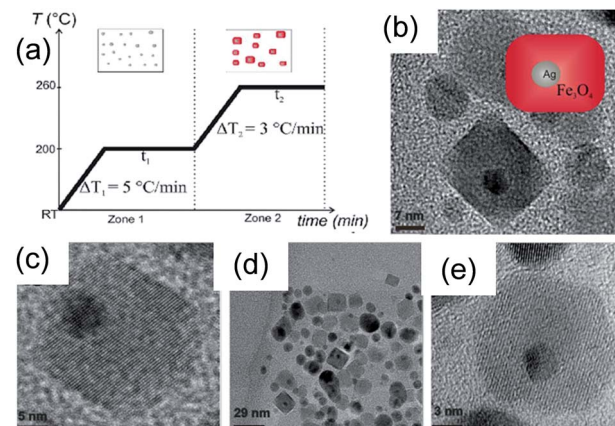


Fig. 13 (a) Temperature profile of the temperature-paused single-step thermal decomposition synthesis. Boxes sketch the expected predominant structures for each time zone. Typically, both waiting times are 120 minutes. Images: TEM images of BLNs obtained following the temperature-paused single-step protocol. Ag corresponds to the dark contrast, while lighter particles correspond to magnetite. Plain magnetite nanoparticles which are formed are also shown in (c). (a) (b) and (d) are different amplifications of BLNs in order to understand the structure. Reprinted with permission from ref. 81. Copyright 2014 Nature.

Ag@Fe₂O₃ yolk@shell NPs by the Kirkendall effect. A facile approach to synthesize rattle type magnetic nanocomposite with a permeable Fe₃O₄ shell and noble metallic core was reported by Xuan *et al.*⁹¹ The formation mechanism involved *in situ* reduction of noble metal NPs followed by transformation of Fe₃O₄ hollow spheres from Fe-complex precursor through an Ostwald ripening process as shown in Fig. 14a.

2.1.5 Metal@Cu₂O core@shell NPs. Au@Cu₂O core@shell nanocubes were first synthesized by Wang *et al.*⁹² using annealing of gold NPs dispersed on a copper grid which involved local Cu oxidation at the Au NPs. Formation of Au@Cu₂O core@shell NPs with precise morphological control of both components was first reported by Huang and coworkers.^{93–95} They have synthesized Au@Cu₂O core@shell NPs using gold nanoplates, nanorods, octahedra, and highly faceted NPs as the structure-directing cores for the overgrowth of Cu₂O shells by a facile aqueous solution approach as shown in Fig. 15.

It has been found that the Au NPs cores have guided the growth of Cu₂O shells with morphological and orientation control. It has been suggested that the {111} planes of Cu₂O were found to grow epitaxially on the {111} facets of gold for most of the cases examined, while the {200} planes of Cu₂O can grow over the {200} facets of gold to form the interfaces. Interestingly, the lattice mismatch between the {111} planes of Au and the {111} planes of Cu₂O is about 4.5%, whereas 4.7% between the {200} planes of Au and the {200} planes of Cu₂O. Their analysis suggested that despite the presence of a significant mismatch between Au and Cu₂O lattice planes, Au@Cu₂O core@shell heterostructures with excellent interfacial epitaxial growth can still be prepared. In similar study, they have used rhombic dodecahedral and edge- and corner truncated gold

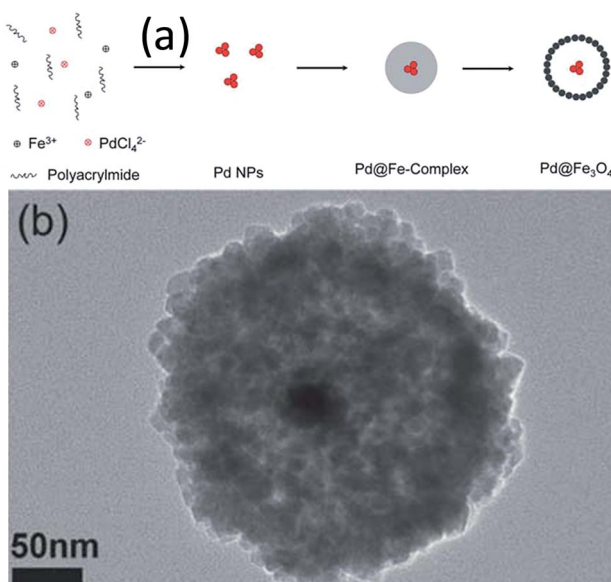


Fig. 14 (a) Schematic illustration of the formation of the rattle type nanostructure and (b) TEM images of the rattle type Pd@Fe₃O₄ nanocomposites. Reprinted with permission from ref. 91. Copyright 2011 Royal Society of Chemistry.

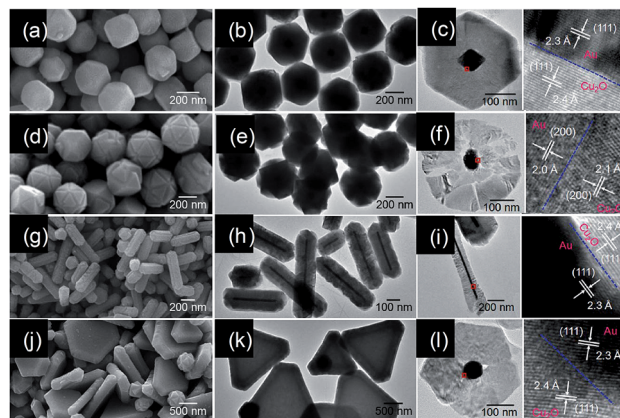


Fig. 15 SEM, TEM, cross-sectional TEM and HRTEM images (red square regions) of the Au@Cu₂O core@shell nanostructures. (a–c) Cuboctahedral heterostructures made from octahedral Au NP cores. (d–f) Truncated stellated icosahedra formed from highly faceted Au NP cores. (g–i) Cu₂O shells with pentagonal prism shape from 5-fold-twinned Au nanorods as templates. (j–l) Thick truncated triangular Cu₂O plates formed from triangular and truncated triangular Au plates as templates. The Cu₂O plates are slightly concave, with thinner central triangular portions. The {111} planes of Cu₂O grow epitaxially on the facets of Au, while the {200} planes of Cu₂O deposit over the {200} facets of Au to form the interfaces. Reprinted with permission from ref. 93. Copyright 2009 American Chemical Society.

nanocrystals with entirely or significant {110} facets as structure-directing cores for the fabrication of Au@Cu₂O core@shell heterostructures with systematic shape evolution (Fig. 16).⁹⁴ By varying the volume of reductant added, shell morphology was systematically tuned from face-raised cubic to cuboctahedral and octahedral structures. They found that the gold cores have an exact orientation relationship with the Cu₂O shells. The {100}, {110}, and {111} faces of the gold nanocrystal cores were parallel to the corresponding faces of the Cu₂O shells.

Zhang *et al.*⁹⁶ have developed a robust wet chemical approach for the highly controllable fabrication of Au@Cu₂O hybrid core@shell and rattle-like yolk@shell NPs. Since then many researchers including our research group have synthesized metal@Cu₂O core@shell NPs for various applications, such as photocatalysis, gas sensors *etc.*^{97–107} In our recent study,¹⁰⁶ Au@Cu₂O core@shell NPs were synthesized by simple solution route and applied for CO sensing applications. Here, Au nanorods (10–15 nm width and 40–60 nm length) were used as core and 30–60 nm Cu₂O shell layer were deposited to form bricks and spherical shape Au@Cu₂O core@shell NPs. The morphology of Au@Cu₂O core@shell NPs was tuned from brick to spherical shape by controlling the pH of the solution. It suggests that core materials are not only the structure directing agent, but synthesis parameters also play an important role. Recently, a novel class of one-dimensional Ag@Cu₂O core@shell heteronanowires has been synthesized at room temperature for photocatalysis application by Xiong *et al.*¹⁰⁸

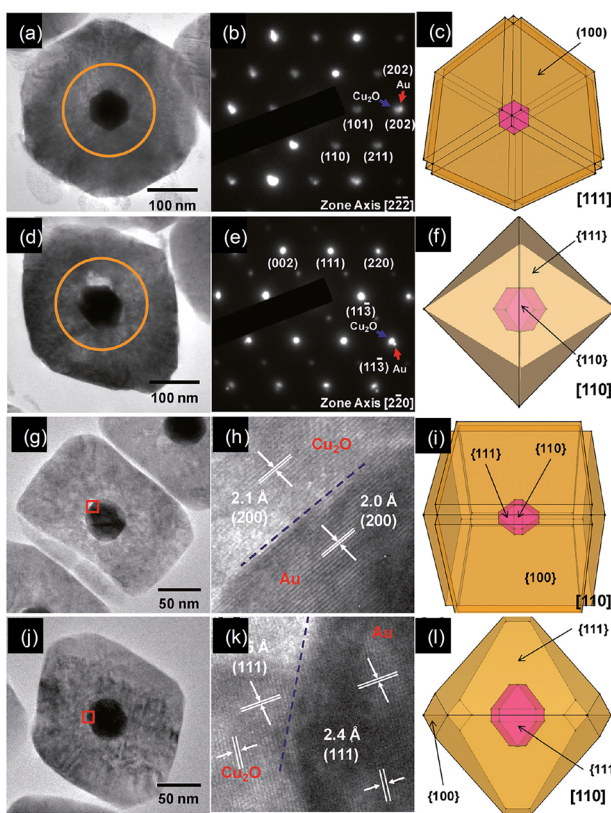


Fig. 16 (a and c) Cross-sectional TEM images of the heterostructures viewed along the [111] and [110] directions and (b and d) SAED patterns of the circled regions in panels a & c of a single Au@Cu₂O core@shell face-raised cube and octahedron using rhombic dodecahedral gold nanocrystal cores. (g and j) Cross-sectional TEM images of the heterostructures viewed along the [110] direction; (h and k) interfacial HRTEM images of the red square regions in panels g & j of a single Au@Cu₂O core@shell face-raised cube and truncated octahedron using edge- and corner-truncated octahedral gold nanocrystal cores; (c, f, i and l) the corresponding drawings. Reprinted with permission from ref. 94. Copyright 2011 American Chemical Society.

2.1.6 Metal@WO₃ core@shell NPs. Ag@WO₃ core@shell nanostructure materials were prepared by a hydrothermal process.^{109,110} Size-controlled Ag NPs with diameter ranging from 25 to 60 nm were synthesized. Ag NPs were dispersed into a Na₂WO₄ solution first, upon adding HNO₃, Ag_x@H₂WO₄ precipitate was formed. An extensive high temperature treatment process was then used to remove water from the precipitate to turn it into Ag_x@WO₃ core@shell. The overall size was ~200 nm and shell thickness was ~60 nm.

2.1.7 Metal@In₂O₃ core@shell NPs. Au@In₂O₃ microstructures with a distinctive core@shell configuration have been successfully synthesized by Li *et al.*¹¹¹ employing Au@carbon spheres (500 nm) as sacrificial templates.¹¹² The growth mechanism suggests that the In³⁺ ions bound with the functional groups (-OH and -C=O groups) present on the carbon surface when these carbonaceous spheres were dispersed in aqueous indium trichloride solutions. Accompany with the following calcination process in air, the carbonaceous templates shrank gradually while the surface layers containing

In³⁺ were condensed to accumulate sufficient mechanical strength to keep the well-defined configuration of spherical NPs (Fig. 17a). After the carbonaceous templates were removed completely, highly crystalline In₂O₃ spheres with closely packed NPs were finally obtained (Fig. 17c). The proposed growth mechanism suggests that the core@shell NPs are formed neither by epitaxial growth of In₂O₃ nor by surfactant stabilization of In₂O₃ on Au NPs, but it is simply a kind of physical adsorption.

2.1.8 Metal@CeO₂ core@shell NPs. The formation of core@shell morphologies of CeO₂ with noble metals has been extensively studied by many researchers.^{113–120} Shinjoh and coworkers^{113,114} reported the synthesis of Ag@CeO₂ core@shell NPs using one-pot selective redox reaction using cerium(III) and silver(I) autocatalyzed by silver metal without the need for surfactants or organic compounds. These core@shell NPs are formed due to aggregation of CeO₂ NPs (14 nm) around Ag NPs (25 nm) and not due to epitaxial growth of CeO₂ on Ag NPs. They claimed it as rice-ball nanostructure because in core@shell structures the shell was composed of polymerized oxide. Similar rice ball type core@shell nanostructures were also reported by other researchers.^{115–117} More recently, Qi *et al.*¹¹⁸ synthesized well-defined Au@CeO₂ core@shell submicrospheres, in which Au NPs core was coated with CeO₂ NPs shell by hydrothermal method.

Au NP core with the diameter of about 17 nm is surrounded with a CeO₂ shell, which was composed of NPs with about 8–10 nm diameter as shown in Fig. 18. The formation mechanism of Au@CeO₂ core@shell submicrospheres suggests that Au³⁺ ions were reduced to Au⁰ by glucose under the hydrothermal condition, which was followed by carbonization of glucose around Au NPs through the dehydration-condensation reaction. The decomposition of urea resulted in the release of OH⁻ ions, which has promoted the adsorption of Ce³⁺ ions with the functional groups of carbon. The calcination of as prepared Au@C@CeO₂ submicrospheres resulted into the burning of

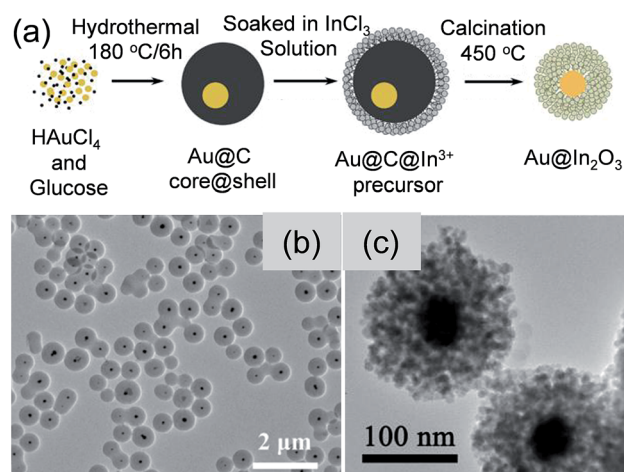


Fig. 17 (a) Schematic formation process of the Au@In₂O₃ core@shell structures. TEM images of (b) Au@C core@shell and (c) Au@In₂O₃ core@shell NPs. Reprinted with permission from ref. 111. Copyright 2014 Royal Society of Chemistry.

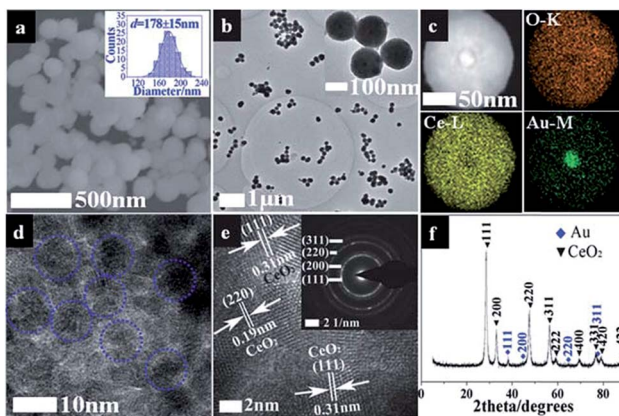


Fig. 18 (a) SEM image of $\text{Au}@\text{CeO}_2$ submicrospheres. The inset is the corresponding size histogram. (b) TEM image of $\text{Au}@\text{CeO}_2$ submicrospheres. The inset is the magnified TEM image. (c) HAADF-STEM mapping image of one submicrosphere. (d) TEM image of the CeO_2 shell of the submicrospheres. (e) HRTEM image of the submicrospheres. The inset is the selected area electron diffraction (SAED) image, indicating the polycrystalline nature of the CeO_2 shell. (f) XRD pattern of the submicrospheres. Reprinted with permission from ref. 118. Copyright 2014 Royal Society of Chemistry.

carbon and simultaneous oxidation of Ce^{3+} ions in the CeO_2 , which leaded in to the formation of $\text{Au}@\text{CeO}_2$ core@shell NPs. It was found that the sizes of Au NP cores were maintained around 17 nm during the calcination process, though the overall sizes of the submicrospheres considerably decreased. This result demonstrates the excellent physical confinement of CeO_2 shells, which effectively prevents possible sintering, migration and growth of Au NP cores. Hollow core@shell NPs have also been synthesized by hydrothermal¹¹⁹ as well as template method.¹²⁰

2.1.9 Metal@ Co_3O_4 core@shell NPs. There are very limited reports on the formation of core@shell NPs of Co_3O_4 using noble metals. For example, Hu *et al.*¹²¹ reported the synthesis $\text{Au}@\text{Co}_3\text{O}_4$ core@shell nanocubes using solvothermal method. However, there is no clear evidence of formation of core@shell formation in these structures. Kim *et al.*¹²² reported the formation of $\text{Au}@\text{Co}_3\text{O}_4$ core@shell nanowires. More recently, Zhuang *et al.*¹²³ synthesized monodisperse $\text{Au}@\text{Co}_3\text{O}_4$ core@shell NPs, which were converted from the oxidation of mono-disperse $\text{Au}@\text{Co}$ core@shell NCs. Apart from this, core@shell NPs with other metal oxides have also been reported, however, none of them have well-defined core@shell structures and uniform sizes.^{124,125}

2.2 Yolk@shell NPs

The yolk@shell nanostructures represent a special class of core@shell structures with a distinctive core@void@shell configuration. The use of template-based routes is an effective approach for the formation of hollow capsules of functional materials. Therefore, a detailed description of the synthesis methodologies of yolk@shell NPs based on template routes is provided in this section.

2.2.1 Metal@metal oxide yolk@shell NPs using metal@ SiO_2 core@shell NPs template. SiO_2 is a representative sacrificial template that is widely used to fabricate noble metal@metal oxide yolk@shell nanostructures.^{126–132} It involved the coating of SiO_2 on pre-synthesized noble metal NPs followed by the target shell materials. Afterwards, the SiO_2 interlayer was etched away selectively with concentrated hydrofluoric acid or an alkaline solution followed by calcination treatment to obtain crystalline yolk@shell nanostructures as shown in Fig. 19.¹²⁸

This versatile method has been used successfully to synthesize various yolk@shell NPs, though the synthesis of yolk@shell structures with the required size, shape, and surface properties is still difficult. Other disadvantages are the partial etching and grain growth. Furthermore, the high production cost of the SiO_2 template method also limits the use of this method at small-scale.

2.2.2 Metal@metal oxide yolk@shell NPs using metal@carbon core@shell NPs template. Similar to SiO_2 , carbon spheres are also widely used as template for the preparation of hollow structure. Mostly glucose was used for the synthesis carbon spheres under hydrothermal reaction.¹¹² Since, glucose is a reducing agent, glucose stabilized noble metals and their subsequent carbonization in hydrothermal reaction produce carbon encapsulated noble metals. We have synthesized $\text{Au}@\text{NiO}$ yolk@shell NPs, for the first time, using $\text{Au}@\text{C}$ core@shell NPs as a template to as shown in Fig. 20a.¹³³ In the NiO coating process, Ni^{2+} ions were binding with the functional groups present on the carbon surface when these carbonaceous spheres were dispersed in aqueous nickel chloride solutions. The removal of carbon through the calcination in the presence of air resulted in the formation of yolk@shell. Similar strategy has also been used for the synthesis of $\text{Au}@\text{ZnO}$ and $\text{Au}@\text{TiO}_2$ yolk@shell NPs.^{134,135}

Despite all the successes in this field, the synthesis of noble metal@metal oxide core@shell NPs often requires multi-step approaches. Thus, the lack of a general method for the synthesis of high quality core@shell NPs with controllable sizes, compositions, shapes, and nano-architectures at a low cost is highly required. The lattice mismatch between metal and metal oxide should be carefully considered to develop a

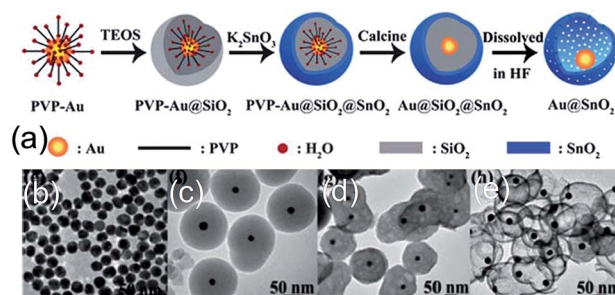


Fig. 19 (a) Synthetic route to $\text{Au}@\text{SnO}_2$ yolk@shell nanospheres. TEM images of the products obtained after each step: (b) Au NPs; (c) $\text{Au}@\text{SiO}_2$ core–shell structures; (d) $\text{Au}@\text{SiO}_2@\text{SnO}_2$ core@shell@shell structures; (e) $\text{Au}@\text{SnO}_2$ yolk@shell structures. Reprinted with permission from ref. 128. Copyright 2013 Royal Society of Chemistry.

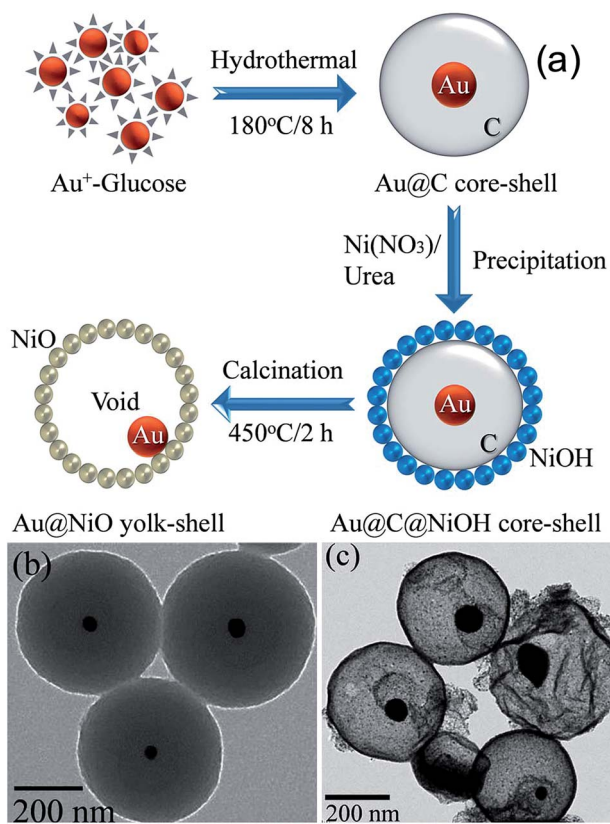


Fig. 20 (a) Schematic presentation of the formation mechanism Au@NiO yolk@shell NPs. TEM images of (b) Au@C core@shell and (c) Au@NiO yolk@shell NPs. Reprinted with permission from ref. 133. Copyright 2014 Royal Society of Chemistry.

generalized method for the synthesis of variety of core@shell NPs. Synthesis of core@shell NPs with multiple cores is another challenge. The yolk@shell NPs with hollow space between core particles and shells can also be used to harvest unique advantages over traditional core@shell NPs. Therefore, it is required to develop a facile synthesis method for core@shell or yolk@shell with control in functionality, size, shape and structure in order to achieve new or enhanced properties.

3. Gas sensing applications of core@shell nanostructures

Herein, we will highlight some existing and potential applications of core@shell NPs, with special focus on their applications in gas sensor. The use of core@shell NPs in gas sensing has been initiated by our research group in our knowledge.²⁵ The gas sensing properties of CO (1000–200 ppm) gas was investigated, which showed higher response ($R_s = (R_a - R_g)/R_a$) for core@shell NPs compared to bare SnO₂ NPs. The higher response of the Au@SnO₂ core@shell NPs was related to the electronic as well as chemical sensitization of Au NPs. Further study of microstructural property of Au@SnO₂ core@shell NPs showed that high porosity within SnO₂ shell layers increased the accessibilities of Au NP to the CO gas molecules and

resulted in high CO responses.⁵³ Since, gas sensor operation involves high temperature, thermal stability of core@shell NPs for high temperature sensing was also examined by our research group using Au@TiO₂ core@shell NPs.³⁶ It is well known that the anatase phase of TiO₂ is highly unstable and start to transform in rutile phase at high temperature, mostly above 500 °C. This phase transition may induce a drift in response at high sensor operating temperatures. However, there was no phase transition from anatase to rutile even after sintering of these Au@TiO₂ core@shell NPs at 900 °C. It indicates the thermal stability of core@shell morphology and sensor at elevated temperature. Furthermore, the response ($R_s = R_a/R_g$) of Au@TiO₂ core@shell NPs was higher as compared to pure TiO₂ at the entire sensing temperatures and concentrations of CO (1000–200 ppm). Since then, several researchers have used core@shell NPs for gas sensor applications.^{54–60} Wu *et al.*⁵⁸ have investigated the sensing mechanism of Ag@SnO₂ core@shell NPs for ethanol (200 ppm) by comparing its gas sensing performance with bare SnO₂ and 1 wt% Ag/SnO₂ nanocomposites. The sensor response ($R_s = R_a/R_g$) of bare SnO₂ was 1.54, and the response and recovery times were 54 s and 85 s, respectively. For 1 wt% Ag/SnO₂ nanocomposites, the sensor response, response and recovery times were 1.24, 52 s and 53 s, respectively. It was found that the Ag@SnO₂ core@shell NPs had a better sensor response of 2.24 and the shorter response and recovery times of 34 s and 68 s, respectively. The lower response of Ag/SnO₂ nanocomposite than that of bare SnO₂ indicates that the silver might block some active sensing sites on the surface of SnO₂. The high response of Ag@SnO₂ core@shell was related to surface area, where the specific surface area of the core@shell structure was higher than that of the bulk material.

To investigate the sensing mechanism they have calculated the adsorption of the C₂H₅OH molecule on Ag@SnO₂ core@shell NPs. It has been found that the adsorption energy of C₂H₅OH on Ag@SnO₂ core@shell NPs is smaller than SnO₂, which is closer to van der Waals' force as shown in Fig. 21a. Furthermore, the magnitude of the exothermic adsorption energy decreases with increasing adsorbed molecules. For example, the distance between an ethanol molecule and the surface of Ag@SnO₂ core@shell NPs was 0.2786 nm when one to ten ethanol molecules were adsorbed (Fig. 21b). This distance was similar to the distance required for a van der Waals' interaction. This resulted in faster desorption of C₂H₅OH for Ag@SnO₂ core@shell NPs as compared to SnO₂, which was responsible for faster recovery time. The faster response of Ag@SnO₂ core@shell NPs was explained on the basis of two ways transfer of electron in Ag@SnO₂ core@shell NPs as compared to one way transfer in SnO₂ which has resulted in lower resistance of Ag@SnO₂ core@shell NPs as compared to SnO₂ (Fig. 21c). Recently, similar result was reported by Chung *et al.*,¹³⁶ where Au@SnO₂ core@shell structures were synthesized by precipitation method and applied for formaldehyde sensing at room temperature. The response ($S = R_{\text{HCHO}}/R_{\text{air}}$) of Au@SnO₂ core shell NPs (2.9) to 50 ppm HCHO was higher compared to Au/SnO₂ composite (2.4) and bare SnO₂ NPs (1.0). Au@SnO₂ core@shell also showed selectivity for formaldehyde

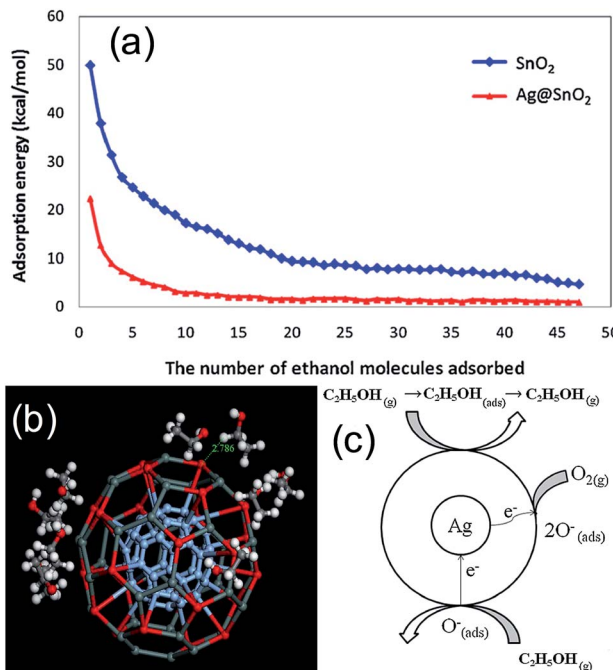


Fig. 21 (a) Exothermic energy of adsorption of each ethanol molecule on SnO_2 and $\text{Ag}@\text{SnO}_2$ surface, (b) simulation of adsorption of ten ethanol ($\text{C}_2\text{H}_5\text{OH}$) molecules on $\text{Ag}@\text{SnO}_2$ [white circles represent hydrogen atoms; black circles represent carbon atoms; red circles represent oxygen atoms; blue circles represent silver atoms; dark green circles represent tin atoms], and (c) mechanism of sensing of $\text{C}_2\text{H}_5\text{OH}$ by $\text{Ag}@\text{SnO}_2$. Reprinted with permission from ref. 58, Copyright 2013 Elsevier.

compared to methanol, ethanol, and NO_2 . Similar result has been reported by other researchers^{109–111,137,138} using different metal oxides for core@shell NPs, where core@shell NPs has shown better performance in terms of high response, fast response and recovery and low operating temperature as compared to bare and noble metal deposited metal oxide NPs.

More recently Xu *et al.*¹¹⁰ have designed and fabricated a localized surface plasmon enhanced chemical sensor based on $\text{Ag}_x@(\text{2D}-\text{WO}_3)$ core@shell NPs. They have synthesized pure WO_3 , Ag_x-WO_3 mixture, and $\text{Ag}_x@(\text{2D}-\text{WO}_3)$ core@shell NPs and investigated their sensing properties (Fig. 22a–d). The combination of the Ag core and the 2D layered structure of WO_3 shell have enhanced sensor performance due to effective localized surface plasmon generation and propagation. The sensor response ($R_s = R_a/R_g$) was increased from 44 for pure WO_3 and 52 for Ag_x-WO_3 mixture to 154 for the $\text{Ag}_x@(\text{2D}-\text{WO}_3)$ core@shell structure towards 500 ppm alcohol. Response and recovery time are also shortened considerably from 3 and 15 s for pure WO_3 , 12 and 7 s for the Ag_x-WO_3 mixture to 2 and 4 s for the $\text{Ag}_x@(\text{2D}-\text{WO}_3)$ core@shell nanostructure. Moreover, optimum sensor working temperature lowered from 370 °C to 340 °C. Thus, the sensors made of $\text{Ag}_x@(\text{2D}-\text{WO}_3)$ core@shell NPs show significantly better performance comparing to those from pure WO_3 and Ag_x-WO_3 mixture. The sensing mechanism was explained on the basis of Schottky barrier formation between n-type WO_3 and Ag NPs. The electrons were transferred

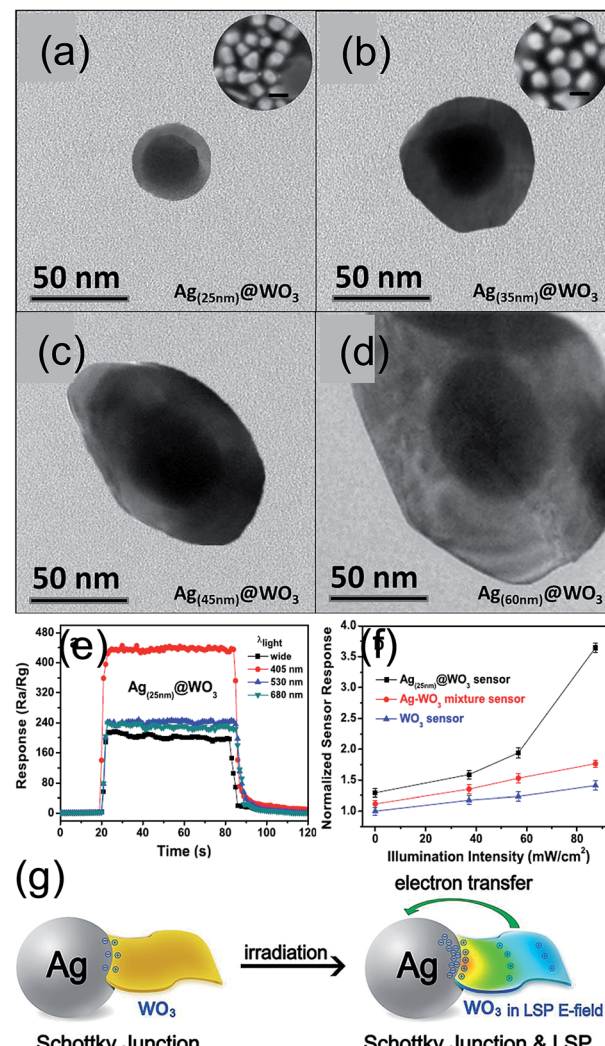


Fig. 22 (a–d) TEM images of $\text{Ag}_x@(\text{2D}-\text{WO}_3)$ core@shell NPs (insets in a and b show the FESEM image of the corresponding Ag NPs with expected diameters). Sensor response under illumination. (e) Sensor response of $\text{Ag}_{(25\text{nm})}@\text{WO}_3$ core@shell NPs at different wavelength of LED irradiation. (f) Normalized sensor response for $\text{Ag}_{(25\text{nm})}@\text{WO}_3$ CSNS, Ag_x-WO_3 mixture and pure WO_3 vs. light illumination intensity using a xenon arc light source (150 W) attenuated using neutral density filters. (g) An illustration of the Schottky junction and LSP enhanced mechanism in $\text{Ag}_x@(\text{2D}-\text{WO}_3)$ based sensors. Reprinted with permission from ref. 110. Copyright 2014 Nature.

from WO_3 to Ag in the $\text{Ag}_x@(\text{2D}-\text{WO}_3)$ core@shell nanostructure due to higher work function of Ag NPs, which resulted in wider depletion zone formation in $\text{Ag}_x@(\text{2D}-\text{WO}_3)$ core@shell as compared to pure WO_3 NPs. Therefore, the response of $\text{Ag}_x@(\text{2D}-\text{WO}_3)$ core@shell was higher as compared to pure WO_3 NPs. The lower response of $\text{Ag}-\text{WO}_3$ mixture as compared to $\text{Ag}_x@(\text{2D}-\text{WO}_3)$ core@shell was explained on the basis of poor Schottky junction formation resulted from relatively long distance between Ag and WO_3 NPs and/or the agglomeration of Ag and WO_3 NPs, as WO_3 powder and Ag NPs were prepared separately before being mixed together. Furthermore, the effect of surface plasmon resonance of Ag NPs on gas sensing has been investigated by light irradiation. They have measured

sensor response as a function of illumination wavelength using LEDs emitting at 405 nm, 530 nm and 680 nm as shown in Fig. 22e. It has been found that the response of $\text{Ag}_x@(\text{2D}-\text{WO}_3)$ sensor was increased after light irradiation especially at blue wavelength where it resonates with the absorption of Ag NPs. The sensor response increases by 188% (from 217 to 408), when irradiated using a 405 nm blue LED, whereas only 10% improvement was observed for 530 nm and 680 nm LEDs irradiation. Furthermore, normalized response for sensors based on $\text{Ag}_{(25 \text{ nm})}@(\text{2D}-\text{WO}_3)$ core@shell, Ag_x-WO_3 mixture and pure WO_3 , were measured at their respective optimum sensor working temperature for 100 ppm alcohol vapor under different illumination ranging from darkness to, 1 sun intensity (Fig. 22f). They found that with increasing light intensity from darkness to 87 mW cm^{-2} resulted in 40% and 60% increase in response of the pure WO_3 and Ag_x-WO_3 mixture, respectively. However, response of $\text{Ag}_{(25 \text{ nm})}@(\text{2D}-\text{WO}_3)$ core@shell NPs increased 308% comparing to its measurement in darkness, which shows its much greater dependence on light intensity. Therefore, the highest increase in response at 405 nm wavelengths clearly suggests that the sensor enhancement is due to the surface plasmon effect of Ag NPs, as surface plasmon wavelength for 25 nm Ag NPs is closer to 405 nm.¹³⁹ Raman study also confirmed this phenomenon as Raman intensity of $\text{Ag}_x@(\text{2D}-\text{WO}_3)$ core@shell NPs was enhanced by 20 times, which is consistent with enhance in sensor performance. Thus, it was proved that localized surface plasmon resonance is a major factor for the enhanced sensor response. This study clearly demonstrates that surface plasmon effect of core metal NPs can be effectively used to boost sensor performance of a core@shell nanostructure and well-defined nanostructures of the shell component are also important to design gas sensors.

However, these studies are focused on n-type metal oxide as shell materials and metal@p-type metal oxide core@shell NPs has not been used for sensing for long time. Recently, our research group and other researchers^{105–107} have reported the use of noble metal@p-type metal oxide core@shell NPs for gas sensing application. Similar to n-type core@shell NPs, p-type core@shell NPs also shows enhanced sensing performance in terms of response, response time, recovery time and lowering of working temperature. For example, Lin *et al.*¹⁰⁷ has synthesized M(Au, Ag, Pd)@ Cu_2O core@shell NPs and investigated the role of noble metals on sensing performance of Cu_2O as shown in Fig. 23a–d. The sensor response ($R_s = R_g/R_a$) to 200 ppm of CO was estimated to be 1.66, 2.61, 1.80, and 2.06 for pure Cu_2O , Au@ Cu_2O , Ag@ Cu_2O and Pd@ Cu_2O nanocrystals, respectively (Fig. 23e). It has been found that the extent of resistance change for CO detection was different in metal@ Cu_2O nanocrystals due to different electron trapping capability of Au, Ag and Pd NPs. The high work function of Au (5.1 eV) and Pd (5.3 eV) as compared to Cu_2O (4.8 eV) resulted in transfer of conduction band electrons of Cu_2O to metal, leaving abundant holes in Cu_2O to increase the hole mobility. For Ag@ Cu_2O nanocrystals, the lower work function of Ag (4.3 eV) has induced electron transfer from Ag to Cu_2O , which formed Schottky barrier at the interface as the thermodynamic equilibrium was reached. Thus, the extent of resistance change upon the exposure to CO was

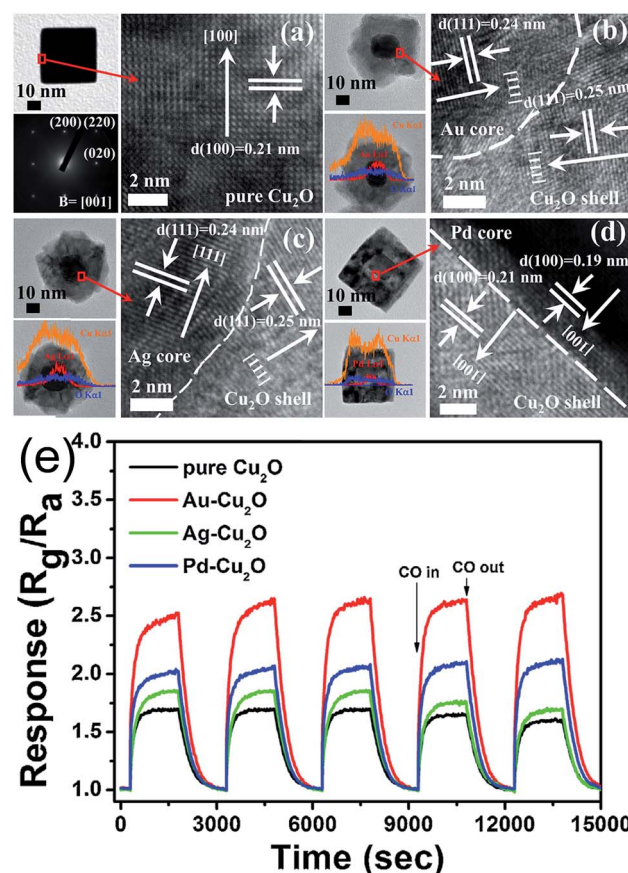


Fig. 23 TEM, HRTEM images and EDS data of (a) pure Cu_2O , (b) $\text{Au}-\text{Cu}_2\text{O}$, (c) $\text{Ag}-\text{Cu}_2\text{O}$ and (d) $\text{Pd}-\text{Cu}_2\text{O}$ nanocrystals; (e) responses of pure Cu_2O and metal@ Cu_2O nanocrystals to 200 ppm of CO recorded at 200°C . Reprinted with permission from ref. 107. Copyright 2014 Elsevier.

enlarged for metal@ Cu_2O nanocrystals as compared to pure Cu_2O , which resulted in increase in response.

Thus, noble metal@metal oxide core@shell NPs have proved their potential for high performance gas sensor application as compared to noble metal decorated metal oxide or pure metal oxide NP. In most studies of n-type MOS gas sensors, the improvement in sensor response was explained by electronic sensitization (increase in depth of depletion layer formation due to Schottky barrier formation) and/or chemical sensitization of noble metals. In electronic sensitization, it has been explained that the increase in air resistance (R_a) of n-type metal oxide due to decrease in carrier density after Schottky barrier formation results in increase in sensor response (R_s) as it is examined either by R_a/R_g or $(R_a - R_g)/R_a$ for reducing gases.^{36,111,138} Similarly, in p-type metal oxide, the response (R_s) is measured either by R_g/R_a or $(R_g - R_a)/R_a$ for reducing gases, and therefore the low R_a value for metal@p-type metal oxide due to increase in hole mobility after Schottky barrier formation results in improvement in response.^{105–107} However, this simple explanation is not always acceptable^{60,107} because the contribution of chemiresistive variation can become relatively more dominant also in p-type oxide semiconductor materials with

lower charge carrier concentration. Moreover, the contribution of chemical sensitization can often become more important in promoting gas sensing reaction. For example, in our recent study,⁶⁰ we have found that the Ag@SnO₂ core@shell NPs showed high response as well as selectivity for *p*-xylene, without considerable effect on other common interfering gases (CO, HCHO, H₂, and NO₂). Based on above explanation, the response of Ag@SnO₂ core@shell NPs for all gases must increase as compared to bare SnO₂. Therefore, it is believed that the enhancement of gas response in noble metal@metal oxides core@shell NPs is more likely due to chemical sensitization rather than electronic gas sensitization. It should be noted that most of p-type MOSs (CuO, Cu₂O, NiO, Cr₂O₃, and Co₃O₄) are good catalysts to oxidize various reducing gases such as ethanol, formaldehyde, benzene, xylene, and toluene because of their abundant oxygen adsorption and easy redox reaction due to multivalent characteristics,⁶ which can be used to design new functionality of gas sensors using core@shell nanostructures.

However, the utilization these core@shell structures as sensing materials in gas sensors may be limited by relatively to

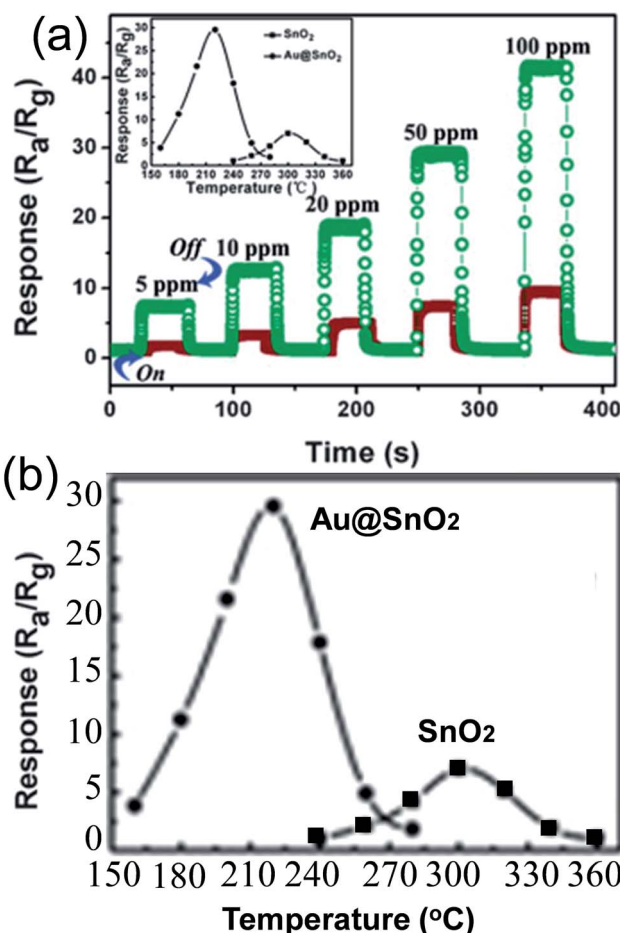


Fig. 24 (a) Responses of Au@SnO₂ yolk@shell and SnO₂ hollow nanospheres for CO at 210 °C and 300 °C and (b) the response of Au@SnO₂ yolk@shell (●) and SnO₂ hollow nanospheres (■) at different operating temperature to 50 ppm of CO (enlarge of inset of (a)). Reprinted with permission from ref. 128, Copyright 2014 Royal Society of Chemistry.

low accessibility of metal NPs to gas molecules. Therefore, a hybrid of core@shell structure, Au@SnO₂ yolk@shell nanospheres, where Au NPs are effectively separated and highly accessible to gas molecules were synthesized and applied for CO (5–100 ppm) sensing.¹²⁸ Au@SnO₂ sensor displayed about five fold enhancements in sensitivity compared to hollow SnO₂ with lower operating temperature (210 °C), lower detection limit (5 ppm), faster response (0.3 s) and better selectivity (Fig. 24). These improved sensing properties were attributed to the electronic as well as catalytic effect of Au NPs accompanied by unique features of yolk@shell nanospheres, which has provided sufficient active surfaces and accessibility of gas molecules to catalytic Au NPs.

In a similar study, Li *et al.*¹³⁴ has synthesized Au@ZnO yolk@shell nanospheres for gas sensor applications. The response of the Au@ZnO nanospheres was about 2 and 3 times higher than that of ZnO hollow and solid nanostructures, respectively for 100 ppm of acetone as shown in Fig. 25a. The Au@ZnO yolk@shell nanospheres exhibited enhanced responses for each gas compared with that based on pure ZnO hollow nanospheres (Fig. 25b). The enhanced performance of hollow structure as compared to solid one was explained on the basis of distinctive configuration (hollow interiors and porous shells), which has endowed ZnO hollow nanospheres and Au@ZnO composite plenty of pores. This unique structure has facilitated the in-diffusion of the test gas (utility factor) and improved the kinetics of the reaction between the test gas and surface adsorbed oxygen species as shown in Fig. 25c. Again, the better performance of Au@ZnO yolk@shell nanostructure as compared to hollow ZnO nanosphere was attributed to electronic as well as chemical sensitization of Au NPs.

Similar study was performed for p-type metal oxide, where Au@NiO yolk@shell NPs was used for efficient H₂S sensor by

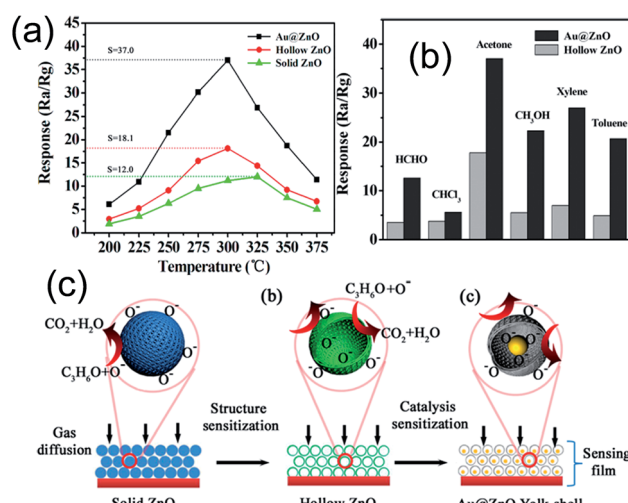


Fig. 25 (a) Responses of the sensor devices upon exposure to 100 ppm acetone at different working temperatures, (b) responses of sensors based on ZnO hollow nanospheres and Au@ZnO yolk@shell nanospheres to various gases (100 ppm), and (c) gas sensing principles of (a) solid ZnO nanospheres, (b) hollow ZnO nanospheres, and (c) Au@ZnO nanospheres. Reprinted with permission from ref. 134, Copyright 2014 American Chemical Society.

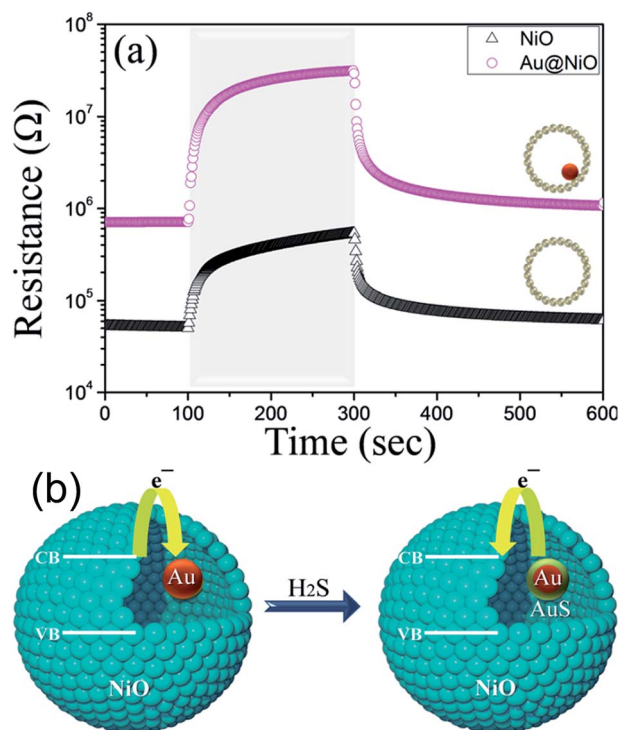


Fig. 26 (a) Response transients of Au@NiO yolk@shell NPs and NiO NPs to 5 ppm H_2S at $400\text{ }^\circ\text{C}$, (b) schematic diagram of H_2S sensing mechanism in Au@NiO yolk@shell NPs. Reprinted with permission from ref. 133, Copyright 2014 Royal Society of Chemistry.

our research group.¹³³ The responses of Au@NiO yolk@shell NPs was approximately 4 times higher than that for pure NiO hollow nanospheres towards 5 ppm H_2S and also showed selectivity for it compared to other interfering gases (ethanol, *p*-xylene, NH_3 , CO and H_2) (Fig. 26a). The improved performance of Au@NiO yolk@shell NPs was attributed to hollow spaces that allowed the high accessibility of Au NPs to gas molecules as well as electronic and chemical sensitization of Au NPs. For selectivity towards H_2S gas, it was suggested that adsorption of H_2S on Au NPs resulted in the formation of sulfide layer, which possibly lowered its work function, and therefore tuned the electron transfer from Au to NiO rather NiO to Au, which resulted in increase in resistance (Fig. 26b). Therefore, the response Au@NiO yolk@shell NPs was increased for H_2S as compared to other gases.

4. Future outlook

In order to further improve the performance of core/yolk@shell NPs in gas sensing applications, it is important to select the components of the core and shell materials with high catalytic activity towards target gas, and also designing of more elaborate structure without affecting the properties of the core/yolk@shell NPs, such as surface area, porosity, electrical conductivity *etc.*, which are possible directions for future studies. The key parameters for controlling the gas performance are discussed below.

A. The electronic sensitization

It controls the charge carrier concentration by transfer of electron between metal and MOS. Therefore, the selection of materials with different work functions should be considered for the design of core@shell NPs. For example, noble metals having lower work function compared to metal oxide will donate the electrons to metal oxides, and therefore lowered its air resistance (R_a) in n-type metal oxides and *vice versa* in p-type metal oxides. Similarly, noble metal having higher work function compared to metal oxide will accept the electron from metal oxides and therefore increase its air resistance in n-type metal oxides and *vice versa* in p-type metal oxides. Therefore, the gas response (R_a/R_g or R_g/R_a) can be controlled by controlling air resistance (Fig. 27).¹⁰⁷

B. The chemical sensitization

It involves the enhancement of gas response, selectivity, and responding kinetics assisted by catalytic promotion of overall/specific gas sensing reaction by core metal NPs. For example, Au shows catalytic activity towards CO, where Pd for H_2 gas, therefore these core metal NPs can be used for the enhancement of gas response for these gases, respectively.^{141,142}

C. The morphological parameters of shell MOS layers

This parameter involves crystallite size (surface to volume ratio, full electron depletion), nano- and meso-porosity of shell layers (for controlling high gas accessibility of shell layers as well as core catalytic metal particles), the overall nanoarchitectures of shell MOS layers, which can be used to improve the gas response and selectivity. For example, smaller the crystallite size, the wider would be depletion layer formation and hence higher would be gas response.⁸ Nano- and meso-porosity could be used for tuning the gas selectivity because it will help in filtering the large gas molecules. The selectivity can also be improved by overall nanoarchitecture of shell, such as exposing the high catalytic active plane of metal oxide in a shell for a particular gas can improve its selectivity (Fig. 28).

D. The morphological parameters of core metal particles

Different morphologies of core as well as multi-core particles can be also considered to enhance the catalytic effect or surface plasmon effect (Fig. 29). For example, core NPs having different crystallographic orientations will show different catalytic activity

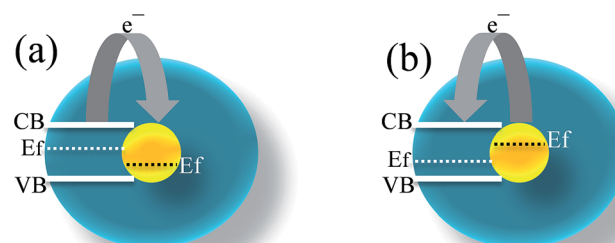


Fig. 27 Electronic sensitization in noble metal@metal oxide core@shell NPs; (a) low work function and (b) high work function of metal oxide compared to noble metal.

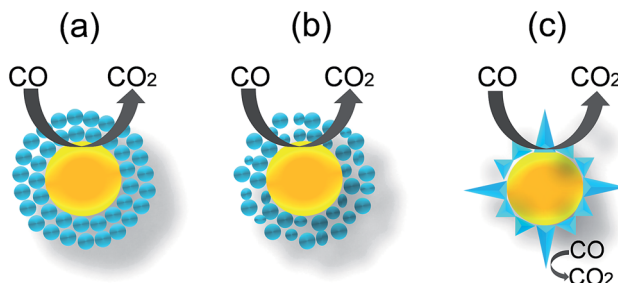


Fig. 28 Noble metal@metal oxide core@shell NPs having different morphologies of shell; (a) uniform size and porosity of shell, (b) non-uniform size and porosity and (c) crystallographic orientation of shell.

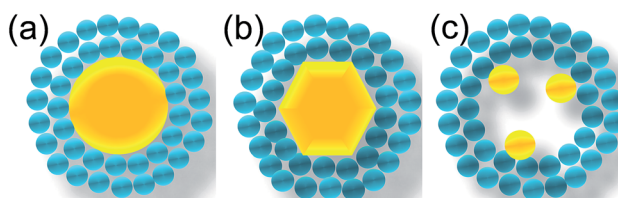


Fig. 29 Noble metal@metal oxide core@shell NPs having different morphologies of core; (a) spherical, (b) hexagonal and (c) multiple cores.

towards target gas. The change in shape also affects the surface plasmon peak position, which can be used to tune the sensor response in a particular wavelength of light.¹⁴³ Furthermore, core@shell NPs having multiple cores can improve the depletion layer formation and also there will be multiple sites for target gas to react, which is expected to improve the gas sensor performance. The presence of multiple cores with different sizes will also affect the surface plasmon band position, which can be used to tune the sensor response in a particular wavelength of light. Bimetallic noble metals (Au–Ag, Au–Pd, Pd–Pt etc.) or their core@shell (Au@Ag, Au@Pt, Au@Pd) can also be used as core materials to improve or tune the sensor performance.^{144,145} For example, bimetallic NPs can show better thermal stability as well as catalytic activity compared to their individual counterpart.¹⁴⁶

E. The volume between shell layer and core metal particles

It can be also used as micro-reactor to reform the analyte gas into more active gases. It has been found in our previous studies that the inwards diffusion of methyl benzene (toluene, xylene) to the underlying layer of the shell close to the catalyst NPs and its dissociation into more active smaller species by catalytic layers are the major factors behind the selective detection of methyl benzene.^{60,147} This can be used another strategy to design new gas sensing materials.

5. Miscellaneous applications of metal@metal oxides core@shell nanostructures

In addition to the applications discussed above, core@shell NPs with different compositions could be used in many other

applications, such as photocatalysis,¹⁸ dye-sensitized solar cells,⁴⁰ catalysis,¹⁹ biological,⁹⁰ and surface enhanced Raman spectroscopy (SERS).¹⁴⁰ For examples, core@shell NPs are showing great potential for photocatalytic application, especially visible light photocatalysis, where surface plasmon phenomenon of noble metals (Au, Ag) has been used for visible light harvesting.^{34,43,47–50} Surface plasmon phenomenon of noble metals in the form of core@shell is also used for efficiency enhancement of dye-sensitized solar cells (DSSC).^{40,42,46} Core@shell NPs have many potential applications in many different fields given their unique properties.

6. Conclusions

In this feature article, we have summarized the potential applications of core@shell NPs in gas sensing. In the past decade, various synthesis approaches have been developed for the preparation of core@shell NPs. Many exciting research contributions are highlighted in this overview, which includes various strategies for the synthesis of core@shell NPs with controllable sizes, shapes, compositions and architectures, and the design of new yolk@shell NPs for gas sensing applications, to illustrate the importance of core@shell NPs. These core@shell NPs have shown better sensing properties as compared to pure metal oxide as well as noble metal deposited metal oxides. The formation of metal oxide shell has provided thermal as well as chemical stability to noble metals. The surface plasmon resonance of noble metals can be used to further improve the gas sensing properties of core@shell NPs under light illumination. In order to harvest unique advantages of core@shell NPs, it is necessary to develop a general and facile method for the synthesis of high quality core@shell NPs with control in functionality, size, shape and structure at a low cost. The core@shell NPs are new and promising platform for high performance gas sensors because physical and chemical properties of core and shell NPs can be tuned or designed separately.

Acknowledgements

This study was supported by Department of Science and Technology (DST), New Delhi, India vide DST-INSPIRE Faculty Scheme (DST/INSPIRE/04/2014/001318).

Notes and references

- 1 D. D. Lee and D. S. Lee, *IEEE Sens. J.*, 2001, **1**, 214–224.
- 2 G. Korotcenkov, *Mater. Sci. Eng., B*, 2007, **139**, 1–23.
- 3 T. Seiyama, A. Kato, K. Fujiishi and M. Nagatani, *Anal. Chem.*, 1962, **34**, 1502–1503.
- 4 N. Taguchi, Jpn. Pat. Appl., S45–38200, 1962.
- 5 <http://www.figarosensor.com/>.
- 6 H. J. Kim and J. H. Lee, *Sens. Actuators, B*, 2014, **192**, 607–627.
- 7 Y. B. Hahn, R. Ahmad and N. Tripathy, *Chem. Commun.*, 2012, **48**, 10369–10385.
- 8 N. Yamazoe, G. Sakai and K. Shimano, *Catal. Surv. Asia*, 2003, **7**, 63–75.

- 9 J. Wöllensteiner, H. Böttner, M. Jaegle, W. J. Becker and E. Wagner, *Sens. Actuators, B*, 2007, **70**, 196–202.
- 10 Z. Jhang and K. Colbow, *Sens. Actuators, B*, 2007, **40**, 47–52.
- 11 P. Montmeat, C. Pijolat, G. Tournier and J. P. Viricelle, *Sens. Actuators, B*, 2002, **84**, 148–159.
- 12 M. Hübner, D. Ko ziej, J. D. Grunwaldt, U. Weimar and N. Barsan, *Phys. Chem. Chem. Phys.*, 2012, **14**, 13249–13254.
- 13 S. Matsushima, Y. Teraoka, N. Miura and N. Yamazoe, *Jpn. J. Appl. Phys.*, 1988, **27**, 1798–18002.
- 14 P. M. Arnal, M. Comotti and F. Schüth, *Angew. Chem., Int. Ed.*, 2006, **45**, 8224–8227.
- 15 V. Subramanian, E. E. Wolf and P. V. Kamat, *Langmuir*, 2003, **19**, 469–474.
- 16 R. G. Chaudhuri and S. Paria, *Chem. Rev.*, 2012, **112**, 2373–2433.
- 17 W. Schärtl, *Nanoscale*, 2010, **2**, 829–843.
- 18 N. Zhang, S. Liu and Y. J. Xu, *Nanoscale*, 2012, **4**, 2227–2238.
- 19 G. Li and Z. Tang, *Nanoscale*, 2014, **6**, 3995–4011.
- 20 J. Liu, S. Z. Qiao, J. S. Chen, X. W. Lou, X. Xing and G. Q. Lu, *Chem. Commun.*, 2011, **47**, 12578–12591.
- 21 M. Giersig, T. Ung, L. M. Liz-Marzan and P. Mulvaney, *Adv. Mater.*, 1997, **9**, 570–575.
- 22 B. O. Dabbousi, J. Rodriguez-Viejo, F. V. Mikulec, J. R. Heine, H. Mattoussi, R. Ober, K. F. Jensen and M. G. Bawendi, *J. Phys. Chem. B*, 1997, **101**, 9463–9475.
- 23 T. Ung, L. M. Liz-Marzan and P. Mulvaney, *J. Phys. Chem. B*, 1999, **103**, 6770–6773.
- 24 S. J. Oldenberg, R. D. Averitt, S. L. Westcott and N. J. Halas, *Chem. Phys. Lett.*, 1998, **288**, 243–247.
- 25 Y. T. Yu and P. Dutta, *Sens. Actuators, B*, 2011, **157**, 444–449.
- 26 D. Li, Q. He and J. Li, *Adv. Colloid Interface Sci.*, 2009, **149**, 28–38.
- 27 H. Zou, S. Wu and J. Shen, *Chem. Rev.*, 2008, **108**, 3393–3957.
- 28 C. Sanchez, B. Julián, P. Belleville and M. Popall, *J. Mater. Chem.*, 2005, **15**, 3559–3592.
- 29 P. Reiss, M. Protière and L. Li, *Small*, 2009, **5**, 154–168.
- 30 A. Guerrero-Martínez, J. Pérez-Juste and L. M. Liz-Marzán, *Adv. Mater.*, 2010, **22**, 1182–1195.
- 31 Y. T. Yu and P. Mulvaney, *Mater. Trans.*, 2004, **45**, 964–967.
- 32 H. W. Kwon, Y. M. Lim, S. K. Tripathy, B. G. Kim, M. S. Lee and Y. T. Yu, *Jpn. J. Appl. Phys.*, 2007, **46**, 2567–2570.
- 33 J. Li and H. C. Zeng, *Angew. Chem., Int. Ed.*, 2005, **44**, 4342–4345.
- 34 X. F. Wu, H. Y. Song, J. M. Yoon, Y. T. Yu and Y. F. Chen, *Langmuir*, 2009, **25**, 6438–6447.
- 35 M. K. Song, P. Rai, K. J. Ko, S. H. Jeon, B. S. Chon, C. H. Lee and Y. T. Yu, *RSC Adv.*, 2014, **4**, 3529–3535.
- 36 Y. S. Kim, P. Rai and Y. T. Yu, *Sens. Actuators, B*, 2013, **186**, 633–639.
- 37 D. A. H. Hanaor and C. C. Sorrell, *J. Mater. Sci.*, 2011, **46**, 855–874.
- 38 P. I. Gouma and M. J. Mills, *J. Am. Ceram. Soc.*, 2001, **84**, 619–622.
- 39 R. D. Shannon and J. A. Pask, *Am. Mineral.*, 1964, **49**, 1707–1717.
- 40 J. Du, J. Qi, D. Wang and Z. Tang, *Energy Environ. Sci.*, 2012, **5**, 6914–6918.
- 41 Z. W. Seh, S. Liu, S. Y. Zhang, K. W. Shah and M. Y. Han, *Chem. Commun.*, 2011, **47**, 6689–6691.
- 42 W. L. Liu, F. C. Lin, Y. C. Yang, C. H. Huang, S. Gwo, M. H. Huang and J. S. Huang, *Nanoscale*, 2013, **5**, 7953–7962.
- 43 J. Goebel, J. B. Joo, M. Dahl and Y. Yin, *Catal. Today*, 2014, **225**, 90–95.
- 44 D. Zhang, X. Song, R. Zhang, M. Zhang and F. Liu, *Eur. J. Inorg. Chem.*, 2005, 1643–1648.
- 45 P. Wang, D. Wang, T. Xie, H. Li, M. Yang and X. Wei, *Mater. Chem. Phys.*, 2008, **109**, 181–183.
- 46 J. Qi, X. Dang, P. T. Hammond and A. M. Belcher, *ACS Nano*, 2011, **5**, 7108–7116.
- 47 B. Cheng, Y. Le and J. Yu, *J. Hazard. Mater.*, 2010, **177**, 971–977.
- 48 X. F. Wu, Y. F. Chen, J. M. Yoon and Y.-T. Yu, *Mater. Lett.*, 2010, **64**, 2208–2210.
- 49 N. Zhang, S. Liu, X. Fu and Y. J. Xu, *J. Phys. Chem. C*, 2011, **115**, 9136–9145.
- 50 N. Zhou, L. Polavarapu, N. Gao, Y. Pan, P. Yuan, Q. Wang and Q. H. Xu, *Nanoscale*, 2013, **5**, 4236–4241.
- 51 G. Oldfield, T. Ung and P. Mulvaney, *Adv. Mater.*, 2000, **12**, 1519–1522.
- 52 Y. T. Yu and P. Dutta, *J. Solid State Chem.*, 2011, **184**, 312–316.
- 53 T. Yanagimoto, Y. T. Yu and K. Kaneko, *Sens. Actuators, B*, 2012, **166–167**, 31–35.
- 54 S. K. Tripathy, A. Mishra, S. K. Jha, R. Wahab and A. A. Al-Khedhairy, *Anal. Methods*, 2013, **5**, 1456–1462.
- 55 K. Yu, Z. Wu, Q. Zhao, B. Li and Y. Xie, *J. Phys. Chem. C*, 2008, **112**, 2244–2247.
- 56 K. K. Haldar and A. Patra, *Chem. Phys. Lett.*, 2008, **462**, 88–91.
- 57 S. K. Tripathy, H. W. Kwon, Y. M. Leem, B. G. Kim and Y.-T. Yu, *Chem. Phys. Lett.*, 2007, **442**, 101–104.
- 58 R. J. Wu, D. J. Lin, M. R. Yu, M. H. Chen and H. F. Lai, *Sens. Actuators, B*, 2013, **178**, 185–191.
- 59 S. Das, S. Sinha, B. Das, S. K. Suar, S. K. S. Parashar, M. Mohapatra, A. Mishra and S. K. Tripathy, *J. Mater. Sci.: Mater. Electron.*, 2014, **25**, 217–223.
- 60 P. Rai, S. M. Majhi, Y. T. Yu and J. H. Lee, *RSC Adv.*, 2015, **5**, 17653–17659.
- 61 Z. L. Wang, *Nano Today*, 2010, **5**, 540–552.
- 62 K. K. Haldar, T. Sen and A. Patra, *J. Phys. Chem. C*, 2008, **112**, 11650–11656.
- 63 F. R. Fan, Y. Ding, D. Y. Liu, Z. Q. Tian and Z. L. Wang, *J. Am. Chem. Soc.*, 2009, **131**, 12036–12037.
- 64 P. Li, Z. Wei, T. Wu, Q. Peng and Y. Li, *J. Am. Chem. Soc.*, 2011, **133**, 5660–5663.
- 65 M. E. Aguirre, H. B. Rodríguez, E. S. Roman, A. Feldhoff and M. A. Grela, *J. Phys. Chem. C*, 2011, **115**, 24967–24974.
- 66 H. R. Liu, G. X. Shao, J. F. Zhao, Z. X. Zhang, Y. Zhang, J. Liang, X. G. Liu, H. S. Jia and B. S. Xu, *J. Phys. Chem. C*, 2012, **116**, 16182–16190.

- 67 X. Yin, W. Que, D. Fei, F. Shen and Q. Guo, *J. Alloys Compd.*, 2012, **524**, 13–21.
- 68 H. Sun, J. He, J. Wang, S. Y. Zhang, C. Liu, T. Sritharan, S. Mhaisalkar, M. Y. Han, D. Wang and H. Chen, *J. Am. Chem. Soc.*, 2013, **135**, 9099–9110.
- 69 L. F. Zhu, H. Wang, X. S. Shen, L. Y. Chen, Y. W. Wang and H. Y. Chen, *Small*, 2012, **8**, 1857–1862.
- 70 Y. Yang, S. Han, G. Zhou, L. Zhang, X. Li, C. Zou and S. Huang, *Nanoscale*, 2013, **5**, 11808–11819.
- 71 Y. Qin, Y. Zhou, J. Li, J. Ma, D. Shi, J. Chen and J. Yang, *J. Colloid Interface Sci.*, 2014, **418**, 171–177.
- 72 M. Misra, P. Kapur and M. L. Singla, *Appl. Catal., B*, 2014, **150–151**, 605–611.
- 73 M. Misra, P. Kapur, M. K. Nayak and M. L. Singla, *New J. Chem.*, 2014, **38**, 4197–4203.
- 74 L. Arroyo-Ramírez, C. Chen, M. Cargnello, C. B. Murray, P. Fornasiero and R. J. Gorte, *J. Mater. Chem. A*, 2014, **2**, 19509–19514.
- 75 C. Xu, J. Xie, D. Ho, C. Wang, N. Kohler, E. G. Walsh, J. R. Morgan, Y. E. Chin and S. Sun, *Angew. Chem., Int. Ed.*, 2008, **47**, 173–176.
- 76 H. Liu, J. H. Wu, J. H. Min and Y. K. Kim, *J. Alloys Compd.*, 2012, **537**, 60–64.
- 77 G. Lopes, J. M. Vargas, S. K. Sharma, F. Béron, K. R. Pirota, M. Knobel, C. Rettori and R. D. Zysler, *J. Phys. Chem. C*, 2010, **114**, 10148–10152.
- 78 T. D. Schladt, M. I. Shukoor, K. Schneider, M. N. Tahir, F. Natalio, I. Ament, J. Becker, F. D. Jochum, S. Weber, O. Köhler, P. Theato, L. M. Schreiber, C. Sönnichsen, H. C. Schröder, W. E. G. Müller and W. Tremel, *Angew. Chem., Int. Ed.*, 2010, **49**, 3976–3980.
- 79 W. Jiang, Y. Zhou, Y. Zhang, S. Xuan and X. Gong, *Dalton Trans.*, 2012, 4594–4601.
- 80 Y. Zhang, H. Ding, Y. Liu, S. Pan, Y. Luo and G. Li, *J. Mater. Chem.*, 2012, **22**, 10779–10786.
- 81 M. E. F. Brollo, R. López-Ruiz, D. Muraca, S. J. A. Figueroa, K. R. Pirota and M. Knobel, *Sci. Rep.*, 2014, **4**, 6839.
- 82 N. D. Cuonga, T. T. Hoa, D. Q. Khieu, T. D. Lam, N. D. Hoa and N. V. Hieu, *J. Alloys Compd.*, 2012, **523**, 120–126.
- 83 X. Teng, D. Black, N. J. Watkins, Y. Gao and H. Yang, *Nano Lett.*, 2003, **3**, 261–264.
- 84 Y. J. Baek, Q. Hu, J. W. Yoo, Y. J. Choi, C. J. Kang, H. H. Lee, S. H. Min, H. M. Kim, K. B. Kim and T. S. Yoon, *Nanoscale*, 2013, **5**, 772–779.
- 85 Y. Sun, B. Yang, Y. Tian, G. Guo, W. Cai, M. He and Y. Liu, *Micro Nano Lett.*, 2011, **6**, 82–85.
- 86 H. Yin, Z. Ma, M. Chi and S. Dai, *Catal. Today*, 2011, **160**, 87–95.
- 87 K. S. Chou, M. Y. Lin and H. H. Wu, *J. Taiwan Inst. Chem. Eng.*, 2013, **44**, 228–232.
- 88 Y. Chen, N. Gao and J. Jiang, *Small*, 2013, **9**, 3242–3246.
- 89 E. V. Shevchenko, M. I. Bodnarchuk, M. V. Kovalenko, D. V. Talapin, R. K. Smith, S. Aloni, W. Heiss and A. P. Alivisatos, *Adv. Mater.*, 2008, **20**, 4323–4329.
- 90 Z. Wei, Z. Zhou, M. Yang, C. Lin, Z. Zhao, D. Huang, Z. Chen and J. Gao, *J. Mater. Chem.*, 2011, **21**, 16344–16348.
- 91 S. Xuan, Y. Zhou, H. Xu, W. Jiang, K. C. F. Leung and X. Gong, *J. Mater. Chem.*, 2011, **21**, 15398–15404.
- 92 Y. Q. Wang, K. Nikitin and D. W. McComb, *Chem. Phys. Lett.*, 2008, **456**, 202–205.
- 93 C. H. Kuo, T. E. Hua and M. H. Huang, *J. Am. Chem. Soc.*, 2009, **131**, 17871–17878.
- 94 W. C. Wang, L. M. Lyu and M. H. Huang, *Chem. Mater.*, 2011, **23**, 2677–2684.
- 95 S. C. Hsu, S. Y. Liu, H. J. Wang and M. H. Huang, *Small*, 2015, **11**, 195–201.
- 96 L. Zhang, D. A. Blom and H. Wang, *Chem. Mater.*, 2011, **23**, 4587–4598.
- 97 L. Kong, W. Chen, D. Ma, Y. Yang, S. Liu and S. Huang, *J. Mater. Chem.*, 2012, **22**, 719–724.
- 98 J. Li, S. K. Cushing, J. Bright, F. Meng, T. R. Senty, P. Zheng, A. D. Bristow and N. Wu, *ACS Catal.*, 2013, **3**, 47–51.
- 99 S. K. Cushing, J. Li, F. Meng, T. R. Senty, S. Suri, M. Zhi, M. Li, A. D. Bristow and N. Wu, *J. Am. Chem. Soc.*, 2012, **134**, 15033–15041.
- 100 D. Y. Liu, S. Y. Ding, H. X. Lin, B. J. Liu, Z. Z. Ye, F. R. Fan, B. Ren and Z. Q. Tian, *J. Phys. Chem. C*, 2012, **116**, 4477–4483.
- 101 L. Zhang, H. Jing, G. Boisvert, J. Z. He and H. Wang, *ACS Nano*, 2012, **6**, 3514–3527.
- 102 N. Meir, I. J. L. Plante, K. Flomin, E. Chockler, B. Moshofsky, M. Diab, M. Volokh and T. Mokari, *J. Mater. Chem. A*, 2013, **1**, 1763–1769.
- 103 Y. C. Yang, H. J. Wang, J. Whang, J. S. Huang, L. M. Lyu, P. H. Lin, S. Gwo and M. H. Huang, *Nanoscale*, 2014, **6**, 4316–4324.
- 104 H. Jing, N. Large, Q. Zhang and H. Wang, *J. Phys. Chem. C*, 2014, **118**, 19948–19963.
- 105 P. Rai, R. Khan, S. Raj, S. M. Majhi, K. K. Park, Y. T. Yu, I. H. Lee and P. K. Sekhar, *Nanoscale*, 2014, **6**, 581–588.
- 106 S. M. Majhi, P. Rai, S. Raj, B. S. Chon, K. K. Park and Y. T. Yu, *ACS Appl. Mater. Interfaces*, 2014, **6**, 7491–7497.
- 107 Y. K. Lin, Y. J. Chiang and Y. J. Hsu, *Sens. Actuators, B*, 2014, **204**, 190–196.
- 108 J. Xiong, Z. Li, J. Chen, S. Zhang, L. Wang and S. Dou, *ACS Appl. Mater. Interfaces*, 2014, **6**, 15716–15725.
- 109 L. Xu, M. L. Yin and S. Liu, *J. Alloys Compd.*, 2015, **623**, 127–131.
- 110 L. Xu, M. L. Yin and S. Liu, *Sci. Rep.*, 2014, **4**, 6745.
- 111 X. Li, J. Liu, H. Guo, X. Zhou, C. Wang, P. Sun, X. Hu and G. Lu, *RSC Adv.*, 2015, **5**, 545–551.
- 112 X. Sun and Y. Li, *Angew. Chem., Int. Ed.*, 2004, **43**, 597–601.
- 113 T. Kayama, K. Yamazaki and H. Shinjoh, *J. Am. Chem. Soc.*, 2010, **132**, 13154–13155.
- 114 K. Yamazaki, T. Kayama, F. Dong and H. Shinjoh, *J. Catal.*, 2011, **282**, 289–298.
- 115 T. Mitsudome, Y. Mikami, M. Matoba, T. Mizugaki, K. Jitsukawa and K. Kaneda, *Angew. Chem., Int. Ed.*, 2012, **51**, 136–139.
- 116 T. Mitsudome, M. Matoba, T. Mizugaki, K. Jitsukawa and K. Kaneda, *Chem.-Eur. J.*, 2013, **19**, 5255–5258.
- 117 X. Wang, D. Liu, S. Song and H. Zhang, *J. Am. Chem. Soc.*, 2013, **135**, 15864–15872.

- 118 J. Qi, J. Chen, G. Li, S. Li, Y. Gao and Z. Tang, *Energy Environ. Sci.*, 2012, **5**, 8937–8941.
- 119 N. Zhang, X. Fu and Y.-J. Xu, *J. Mater. Chem.*, 2011, **21**, 8152–8158.
- 120 N. Zhang and Y.-J. Xu, *Chem. Mater.*, 2013, **25**, 1979–1988.
- 121 J. Hu, Z. Wen, Q. Wang, X. Yao, Q. Zhang, J. Zhou and J. Li, *J. Phys. Chem. B*, 2006, **110**, 24305–24310.
- 122 B. Y. Kim, I.-B. Shim, Z. O. Araci, S. S. Saavedra, O. L. A. Monti, N. R. Armstrong, R. Sahoo, D. N. Srivastava and J. Pyun, *J. Am. Chem. Soc.*, 2010, **132**, 3234–3235.
- 123 Z. Zhuang, W. Sheng and Y. Yan, *Adv. Mater.*, 2014, **26**, 3950–3955.
- 124 K. Maeda, K. Teramura, D. Lu, N. Saito, Y. Inoue and K. Domen, *Angew. Chem., Int. Ed.*, 2006, **45**, 7806–7809.
- 125 N. Sakamoto, H. Ohtsuka, T. Ikeda, K. Maeda, D. Lu, M. Kanehara, K. Teramura, T. Teranishi and K. Domen, *Nanoscale*, 2009, **1**, 106–109.
- 126 P. M. Arnal, M. Comotti and F. Schüth, *Angew. Chem., Int. Ed.*, 2006, **45**, 8224–8227.
- 127 I. Lee, J. B. Joo, Y. Yin and F. Zaera, *Angew. Chem., Int. Ed.*, 2011, **50**, 10208–10211.
- 128 L. Wang, H. Dou, Z. Lou and T. Zhang, *Nanoscale*, 2013, **5**, 2686–2691.
- 129 X. Huang, C. Guo, J. Zuo, N. Zheng and G. D. Stucky, *Small*, 2009, **5**, 361–365.
- 130 C. Galeano, R. Güttel, M. Paul, P. Arnal, A. H. Lu and F. Schüth, *Chem.-Eur. J.*, 2011, **17**, 8434–8439.
- 131 R. Güttel, M. Paul and F. Schüth, *Chem. Commun.*, 2010, **46**, 895–897.
- 132 C. Chen, X. Fang, B. Wu, L. Huang and N. Zheng, *ChemCatChem*, 2012, **4**, 1578–1586.
- 133 P. Rai, J. W. Yoon, H. M. Jeong, S. J. Hwang, C. H. Kwak and J. H. Lee, *Nanoscale*, 2014, **6**, 8292–8299.
- 134 X. Li, X. Zhou, H. Guo, C. Wang, J. Liu, P. Sun, F. Liu and G. Lu, *ACS Appl. Mater. Interfaces*, 2014, **6**, 18661–18667.
- 135 C. K. Ngaw, Q. Xu, T. T. Y. Tan, P. Hu, S. Cao and J. S. C. Loo, *Chem. Eng. J.*, 2014, **257**, 112–121.
- 136 F. C. Chung, R. J. Wu and F. C. Cheng, *Sens. Actuators, B*, 2014, **190**, 1–7.
- 137 Z. Zhu, C. T. Kao and R. J. Wu, *Appl. Surf. Sci.*, 2014, **320**, 348–355.
- 138 S. M. Majhi, P. Rai and Y. T. Yu, *ACS Appl. Mater. Interfaces*, 2015, **7**, 9462–9468.
- 139 L. W. Jang, D. W. Jeon, T. Sahoo, A. Y. Polyakov, B. Sarvanakumar, Y. T. Yu, Y. H. Cho and I. H. Lee, *J. Mater. Chem.*, 2012, **22**, 21749–21753.
- 140 L. Sun, J. He, S. An, J. Zhang and D. Ren, *J. Mol. Struct.*, 2013, **1046**, 74–81.
- 141 H. L. Jiang, B. Liu, T. Akita, M. Haruta, H. Sakurai and Q. Xu, *J. Am. Chem. Soc.*, 2009, **131**, 11302–11303.
- 142 W. Eberhardt, S. G. Louie and E. W. Plummer, *Phys. Rev. B: Condens. Matter Mater. Phys.*, 1983, **28**, 465–477.
- 143 J. Zhang, C. Xi, C. Feng, H. Xia, D. Wang and X. Tao, *Langmuir*, 2014, **30**, 2480–2489.
- 144 O. Rosseler, A. Louvet, V. Keller and N. Keller, *Chem. Commun.*, 2011, **47**, 5331–5333.
- 145 H. M. Song, D. H. Anjum, R. Sougrat, M. N. Hedhili and N. M. Khashab, *J. Mater. Chem.*, 2012, **22**, 25003–25010.
- 146 X. Liu, A. Wang, X. Yang, T. Zhang, C. Y. Mou, D. S. Su and J. Li, *Chem. Mater.*, 2009, **21**, 410–418.
- 147 Y. J. Hong, J. W. Yoon, J. H. Lee and Y. C. Kang, *Chem.-Eur. J.*, 2014, **20**, 2737–2741.